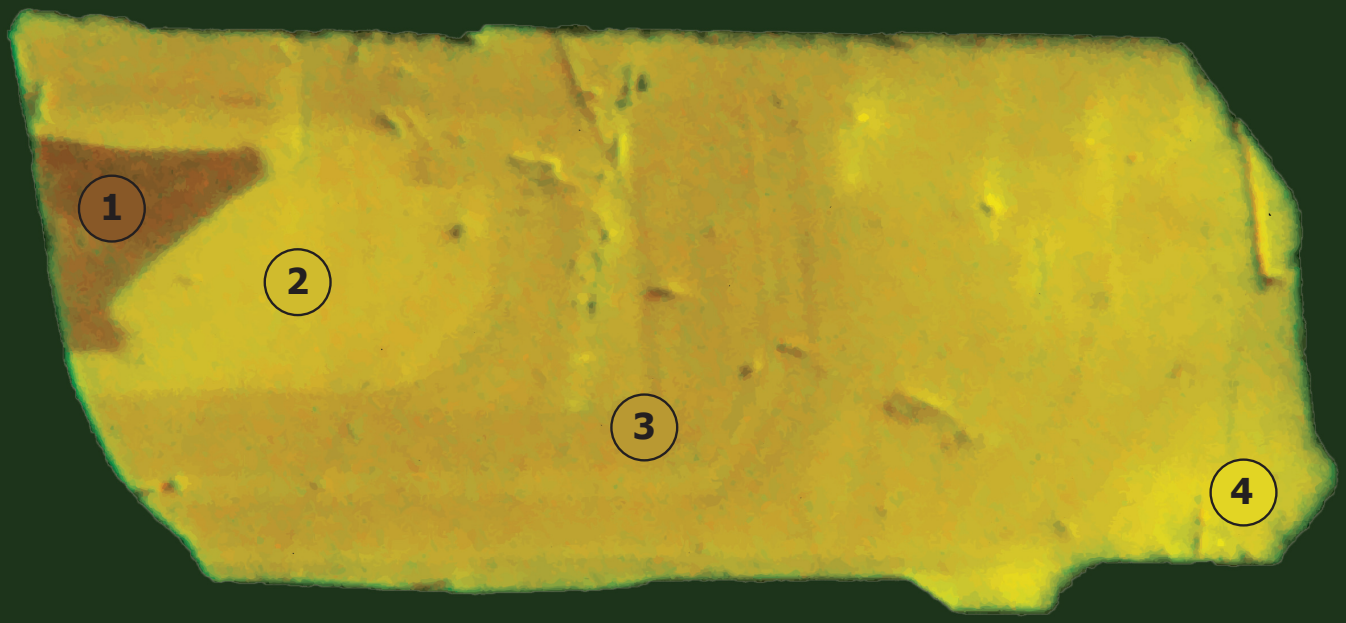

Mineralogical and Geochemical Characteristics of Porphyry-Fertile Plutons: Guichon Creek, Takomkane and Granite Mountain Batholiths, south-central British Columbia

NTS 092I, P, 093A, B

Farhad Bouzari, Craig J.R. Hart, Thomas Bissig and Guillaume Lesage

Geoscience BC Report 2018-17

Geoscience BC

MDRU
MINERAL DEPOSIT RESEARCH UNIT

THE UNIVERSITY OF BRITISH COLUMBIA

Mineralogical and Geochemical Characteristics of Porphyry-Fertile Plutons: Guichon Creek, Takomkane and Granite Mountain Batholiths, south-central British Columbia

NTS 092I, P, 093A, B

Farhad Bouzari, Craig J.R. Hart, Thomas Bissig and Guillaume Lesage

Geoscience BC* Report 2018-17

MDRU Publication 412

Keywords: porphyry indicator minerals, PIMS, porphyry fertility, apatite, titanite, Guichon Creek batholith, Takomkane Batholith, Granite Mountain batholith, British Columbia

Suggested Citation:
Bouzari, F., Hart, C.J.R., Bissig, T., and Lesage, G.(2018): Mineralogical and Geochemical Characteristics of Porphyry-Fertile Plutons: Guichon Creek, Takomkane and Granite Mountain Batholiths, south-central British Columbia (NTS 092I, P, 093A, B); Geoscience BC Report 2018-17, MDRU Publication 412, 36 p.

Report prepared by MDRU†

Dept. Earth, Ocean and Atmospheric Sciences, The University of British Columbia
Vancouver, BC V6T 1Z4, Canada
Tel: +1-604-822-6136
Email: mdru@eoas.ubc.ca

Includes bibliographic references.
Electronic monograph issued in PDF format.
ISBN 978-0-88865-303-1

*Geoscience BC is an independent, non-profit organization that generates earth science in collaboration with First Nations, local communities, government, academia and the resource sector. Our independent earth science enables informed resource management decisions and attracts investment and jobs. Geoscience BC gratefully acknowledges the financial support of the Province of British Columbia.

†MDRU—Mineral Deposit Research Unit is an internationally-recognized collaborative venture between the mining industry and Earth, Ocean and Atmospheric Sciences Department at The University of British Columbia (UBC), established with assistance from the Natural Sciences and Engineering Research Council of Canada (NSERC), and devoted to solving mineral exploration-related problems.

Cover image: Cathodoluminescence image of zoned apatite from the Takomkane Batholith showing luminescence colour variations.

ABSTRACT

Exploration for porphyry copper deposits is mostly focused on following-up on alteration patterns or empirical geochemical or geophysical data, which are ineffective in areas of cover, such as glacial till or regolith. Distinguishing porphyry-fertile from barren plutons in the earliest stages of exploration could provide a significant advantage by immediately identifying those plutons that had the potential to form porphyry copper deposits. This study identifies the mineralogical and geochemical characteristics of porphyry-fertile plutons and develops exploration tools that allow for the identification of such plutonic bodies.

Apatite and titanite are common accessory minerals in felsic intrusive rocks that host porphyry Cu (-Au, Mo) deposits. Textural and compositional features of apatite and titanite grains from three British Columbia batholiths, Guichon Creek (host to Highland Valley deposits), Takomkane (host to Woodjam deposits) and Granite Mountain (host to Gibraltar deposit) are characterized. A total of 581 apatite grains and 689 titanite grains from 41 samples representing various phases of each batholith were analyzed for major and trace elements.

Results show that apatite and titanite from the fertile plutons are characterized by LREE depletion ($(La/Sm)_n < 5$) and commonly by MREE enrichment ((Dy/Yb)n > ca. 1.5). These characteristics result from fractional crystallization of the magma, and subsequent fluid saturation and exsolution.

Porphyry-fertile plutons contain apatite that becomes progressively depleted in chlorine (<0.35 wt.% oxide) and sulphur (<0.3 wt.% oxide) during crystallization. Apatites with higher S and Cl display brown luminescence whereas S- and Cl-depleted apatites have green luminescence.

Titanite from mineralized plutons have high Fe:Al (< 1), which resulted from an increase in oxygen fugacity that controls the abundance of Fe^{3+} that substitutes for Ti, and an increase in Mn that substitutes for Ca. The Eu anomaly in both titanite and apatite is not a robust indication of the oxidation state, rather it is influenced by fractional crystallization.

Sulphur depletion in apatite is attributed to evolution from an early magma that is oxidizing and SO_4-rich, to a melt that is SO_4-poor. The depletion in both Cl and S in apatite from mineralized plutons is evidence of fluid exsolution and subsequent degassing of SO_2-rich magmatic volatiles from SO_4-rich melts. These Cl- and S-rich volatiles generated by fertile plutons are capable of carrying Cu and producing porphyry copper deposits. Titanite that formed along with these Cl- and S-depleted apatites confirms that conditions become progressively oxidized.

Therefore, apatite and titanite show key magmatic fertility parameters of the necessary ingredients (Cl and S), high oxidation state and water content, and more importantly, the favourable conditions that led to fluid exsolution and degassing to potentially form a porphyry deposit at shallower levels. The combination of these fertility parameters in apatite and titanite can identify porphyry-fertile plutons.

INTRODUCTION

The economic contributions of porphyry copper deposits cannot be overstated because their long lifespans permit high profitability during periods of high metal prices. Exploration approaches for PCDs based on known and predictable characteristics of hypogene and supergene alteration patterns have proved successful but cannot be utilized in areas of cover, particularly transported cover. Therefore, there is a need for the development of new exploration tools that can provide predictive and/or detectable evidence in regions of covered porphyry mineralization. Moreover, there is a need to differentiate between marginal or sub-economic PCD prospects and those with the potential to be developed into profitable deposits. Early decisions, such as on area selection, will influence the deployment of exploration dollars on drill campaigns at the prospect scale. With increasingly deep and covered targets, exploration costs and risks are increasing, so cost-effective, early-stage screening tools are critical advances.

Distinguishing porphyry-fertile from barren plutons provides a significant advantage for exploration for porphyry copper deposits, particularly in British Columbia (BC), where many porphyry systems occur within or around the edges of large batholiths. The fundamental relationship of porphyry Cu (-Au, Mo) deposits with intrusions is well established (e.g., Sillitoe, 1973, 2010), but distinguishing metal-fertile from barren plutons is a significant challenge for explorers. This is largely because porphyritic intrusive rocks are abundant in Cordilleran settings, yet very few of these generated or host ore deposits. Information that contributes such *a priori* knowledge potentially provides early guidance to inform more effectively and efficiently to the exploration process to focus exploration resources to the most prospective targets.

This study investigates district- to batholith-scale fertility indicators of porphyry copper deposits in the Guichon Creek, Takomkane and Granite Mountain batholiths by characterizing the textural and geochemical features of minerals such as apatite and titanite to establish tools and strategies that consider the fertility of porphyry copper magmatism in BC.

Porphyry Fertile Magmas

The most fundamental process in forming large porphyry copper deposits is the exsolution of hydrothermal fluids from magma in large crystallizing batholiths prior to and below the site of porphyry copper deposit formation (Burnham and Ohmoto, 1980; Dilles and Einaudi, 1992). These fluids accumulate Cl, S and metals that preferentially partition from the magma to the fluid, and together they buoyantly stream through pathways in the magma to the upper crust where gases exsolve and expand to break the rock in front of the upwardly migrating volatile-rich magmatic front. The resultant episodic decrease in temperature causes the fluids and condensed gases to deposit silicate and sulphide minerals - these cumulatively form porphyry copper deposits (Fig. 1). Six key parameters (Burnham and Ohmoto, 1980; Audetat and Simon, 2012) influence a magma's ability to form porphyry copper deposits: (1) oxidation state, (2) temperature, (3) water, (4) metal, (5) chlorine and (6) sulphur content.

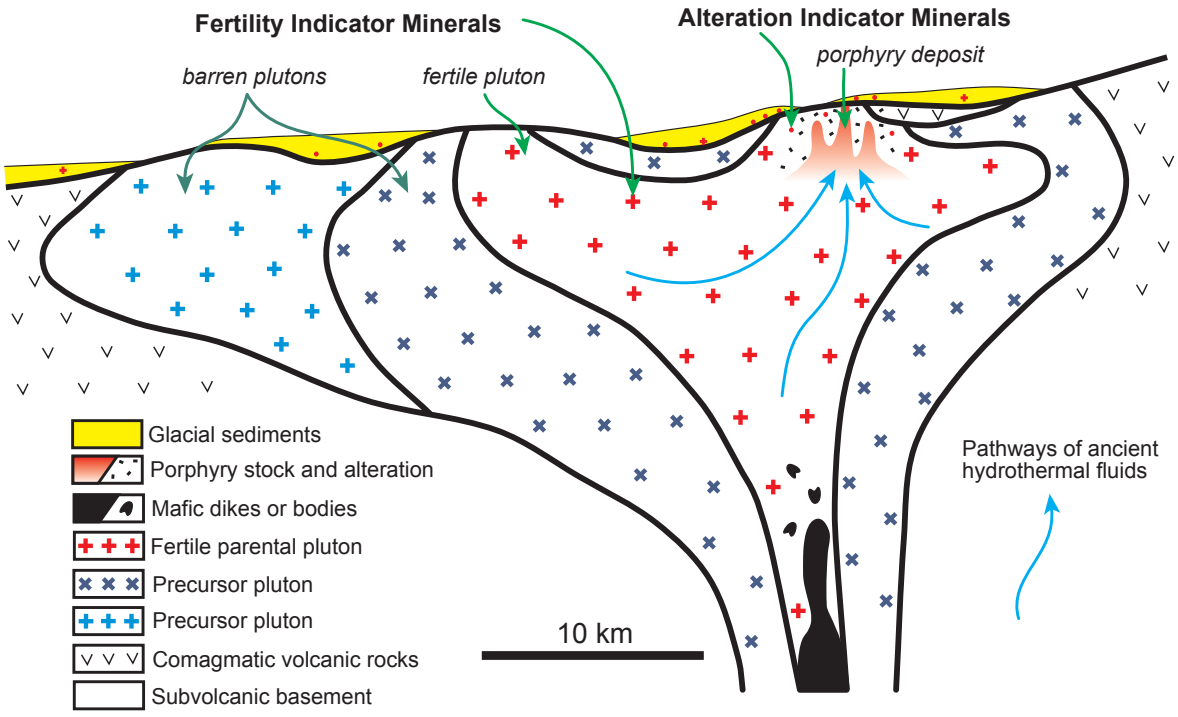

Figure 1: Schematic diagram showing components of a porphyry copper deposit within a composite batholith that is partly covered by sediments. Porphyry indicator minerals will indicate the fertile pluton phase and evidence of typical porphyry alteration and mineralization.

Minerals such as apatite, zircon and titanite have the potential to record the state and trends of these parameters during their growth in the evolving magma. As such, recognition of the presence or robustness of certain magmatic processes associated with porphyry copper deposit formation can indicate the fertility of the parental pluton.

Apatite and Titanite Characteristics as Fertility Minerals

Apatite and titanite are two accessory minerals that typically occur in granitoid rocks and have characteristics that potentially indicate fertility. The apatite mineral structure can incorporate a wide range of transition metals, REE and cations. Sr^{2+}, Mn^{2+}, Fe^{2+}, REE, and Na^{+} substitutions for Ca^{2+} site and Si^{4+}, $As^{5+}$and S^{6+} substitutions for P^{5+} site are common (Elliot, 1994; Waychunas, 2002; Hughes and Rakovan, 2015). Trace-element compositions of apatite ($Ca_5(PO_4)_3(F,Cl,OH)$) have been used to recognize the characteristics of mantle fluids, assimilation, degree of fractionation and the oxidation state of magma (summarized in Bouzari et al., 2016). Zoned magmatic apatite may have S-rich cores that abruptly change to S-poor rims which indicate that early SO_4-rich magma evolved to become SO_4-poor magma due to the crystallization of anhydrite (e.g., Streck and Dilles, 1998).

Apatite is an effective recorder of the chloride content of the crystalizing melt and thus provides an indicator of a magma's ability to potentially transport Cu (Holland, 1972). Apatite associated with porphyry copper deposits tends to be Cl-rich (e.g., Roegge et al., 1974). Mao et al. (2016) showed that apatite compositions can discriminate various host rocks and mineral deposit types. Bouzari et al. (2016) showed that apatite can record differing types of hydrothermal alteration in BC porphyry deposits, using luminescence and chemistry. More recently, Economos et al. (2017) showed that apatite from Cadiz Valley Batholith, CA have high S concentrations and heavy S isotopic ratios in the core while the rims yielded low S concentrations and low isotopic ratios, potentially indicating magma mixing or ascent-driven degassing.

Titanite ($CaTiSiO_5$) is a robust and stable mineral phase in magmatic systems and can incorporate geochemically important trace elements into its structure, thus providing a powerful tool for petrogenetic studies (e.g., Kowallis, 1997; Piccoli et al., 2000) and studies of mineralization–related alteration processes (e.g., Che et al., 2013; Celis, 2015). Several element substitutions can occur within the mineral on the 7-fold coordinated Ca site or the 6-fold coordinated Ti octahedral site. Coupled substitutions such as for REE^{3+}, Fe^{2+}, Fe^{3+} and Al^{3+} are common because the cations that replace Ca and Ti are commonly not the same valancy. In most igneous rocks, the stable Ti-bearing mineral phases are titanomagnetite and ilmenite (Frost and Lindsley, 1991), rather than titanite, indicating that they crystallized at oxygen fugacities too low for the stability of titanite. Titanite forms in relatively oxidized magmatic rocks (Wones, 1989) and is far more likely to be found in the presence of hornblende than in anhydrous rocks (Frost et al., 2000). Kowallis (1997) proposed that the Fe:Al molar ratio can be used to distinguish titanites from different sources such as metamorphic, hydrothermal, and igneous. More significantly, the Fe:Al ratio of titanite provides a robust indicator of oxidation state. Thus, high fO_2 increases Fe^{3+} and high pressure increases Al^{3+} substituting in the Ti-site (Kowallis, 1997).

GEOLOGICAL SETTING

The Quesnel Terrane in south-central British Columbia is characterized by a Late Triassic to Early Jurassic island arc volcano-sedimentary package with numerous contemporaneous plutons and batholiths, some with associated clusters of porphyry copper deposits (Logan and Mihalynuk, 2014). The plutons and batholiths occur as three arc-parallel belts that progressively young from west to east (Fig. 2, Schiarizza, 2015). The western Late Triassic belt is characterized by the calc-alkaline Guichon Creek and Granite Mountain granodioritic batholiths, which host the Highland Valley and Gibraltar porphyry copper districts, respectively. Similar plutonic rock types and potentially porphyry deposits are expected to occur beneath the Neogene and Quaternary cover rocks. The central plutonic belt consists of latest Triassic alkaline plutons that are dominated by monzonitic lithologies including the Copper Mountain, Iron Mask and Mount Polley composite intrusions and related porphyry Cu-Au deposits. The easternmost belt consists of several Early Jurassic calc-alkaline granodioritic batholiths such as the Pennask and Takomkane batholiths which host the Brenda and Woodjam Southeast Zone porphyry deposits, respectively.

This study focuses on establishing the fertility characteristics of plutons that are known to be genetically associated with porphyry copper deposits and clusters. Sample localities were chosen across differing geological settings, rock types and porphyry systems. The Guichon Creek, Granite Mountain and Takomkane batholiths, were chosen for this study. Each batholith is well-documented and mapped (McMillan et al., 2009; Schiarizza et al., 2013; Schiarizza, 2015). In this study, we did not use rocks from commonly small volume but highly-altered porphyry bodies or dikes that commonly occur with the main stage of the alteration and mineralization. Because such intrusive rocks are typically altered, the textural and chemical fertility parameters are likely obliterated or changed by the effect of hydrothermal fluids. Instead we focused on samples from larger plutons that host the porphyry deposits and/or occur within or below the porphyry deposits, and are the likely progenitor magma bodies to the smaller 'porphyry' intrusions. The relationships of such plutons to the porphyry mineralization are thought to be equivalent to the Luhr Hill granite and the Ann Mason deposit at Yerington, Nevada (Dilles and Einaudi, 1992). Even though the link between porphyry mineralization and the hosting pluton are not always fully understood, the close timing

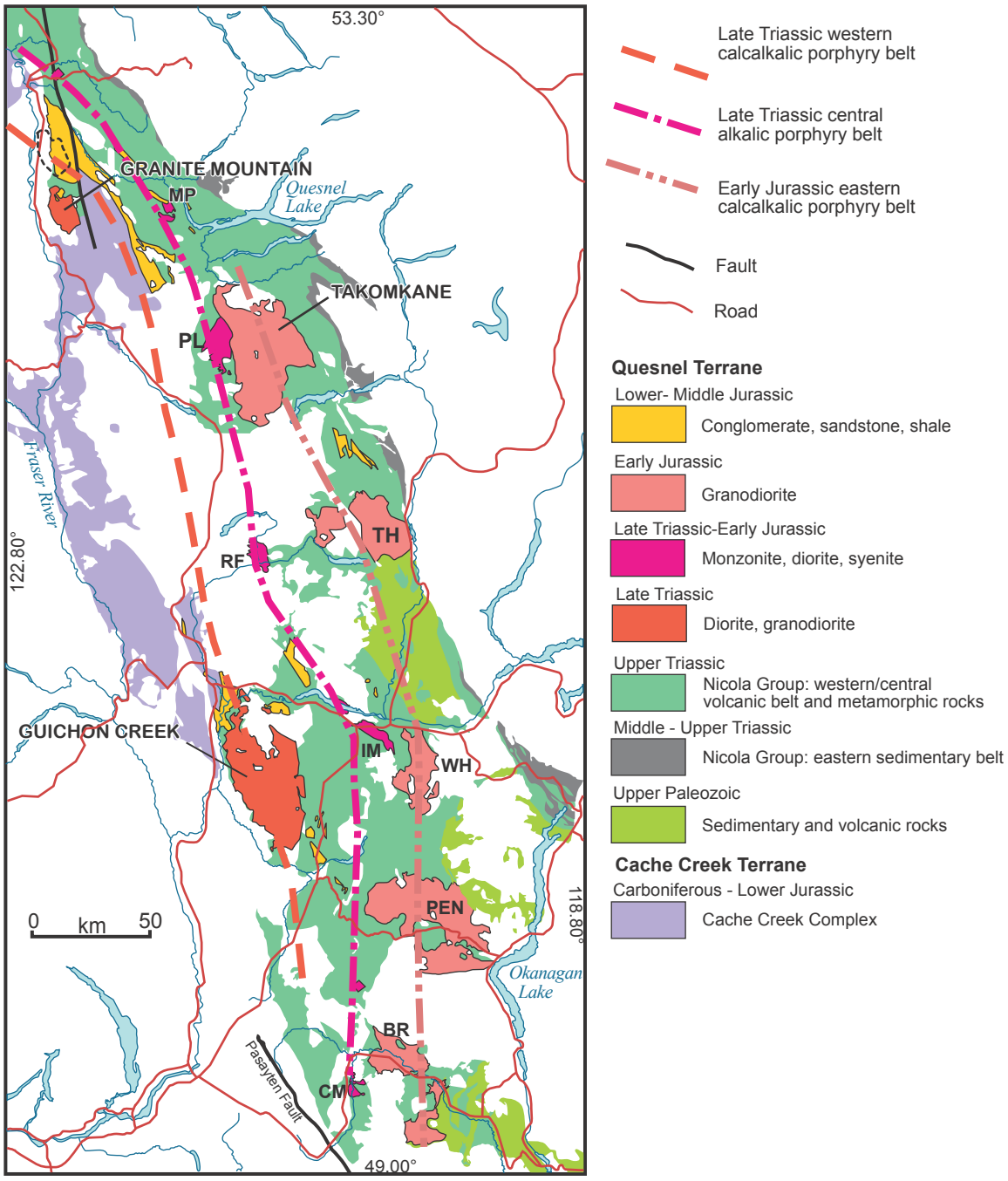

Figure 2: Map of the southern Quesnel and Cache Creek terranes in south-central British Columbia showing the location of major plutonic bodies and porphyry belts (after Schiarizza, 2015). Other shown batholiths: CM = Copper Mountain, IM = Iron Mask, RF = Rayfield River, PL = Peach Lake – Murphy Lake, MP = Mount Polley, BR = Bromley, PEN = Pennask, WH = Wild Horse, TH = Thuya.

relationship and field relationships such as local alteration and mineralization are used to identify mineralized fertile plutons from non-mineralized plutons.

Guichon Creek Batholith

The Late Triassic Guichon Creek batholith (Fig. 3) is a north-trending, approximately 65 x 30 km body that intruded and thermally metamorphosed the Upper Triassic Nicola Group basaltic to andesitic volcanic and volcaniclastic rocks (McMillan et al., 1995) of Quesnel Terrane. The batholith is composite and zoned, with earlier diorite and quartz diorite border phases that surround younger granodiorite phases in the centre (Casselman et al., 1995; Byrne et al., 2013, D'Angelo et al., 2017). These mostly concentric phases, from the margins inward, are: the Border phase, the Highland Valley phases (consisting of Guichon and Chataway subphases), the Bethlehem phases (consisting of Bethlehem and Skeena subphases) and the Bethsaida phase (Fig. 4) The Bethlehem and Skeena subphases and the Bethsaida phase host most of the Highland Valley porphyry Cu-Mo deposits (Valley, Lornex, Highmont, Alwin, Bethlehem and JA). Two mineralization events are recognized: an older Bethlehem phase-related event that formed the Bethlehem area deposits; and the subsequent Valley, Lornex and Highmont deposit-forming event that occurred in conjunction with the emplacement of the Skeena and Bethsaida phases (Byrne et al., 2013, D'Angelo et al., 2017).

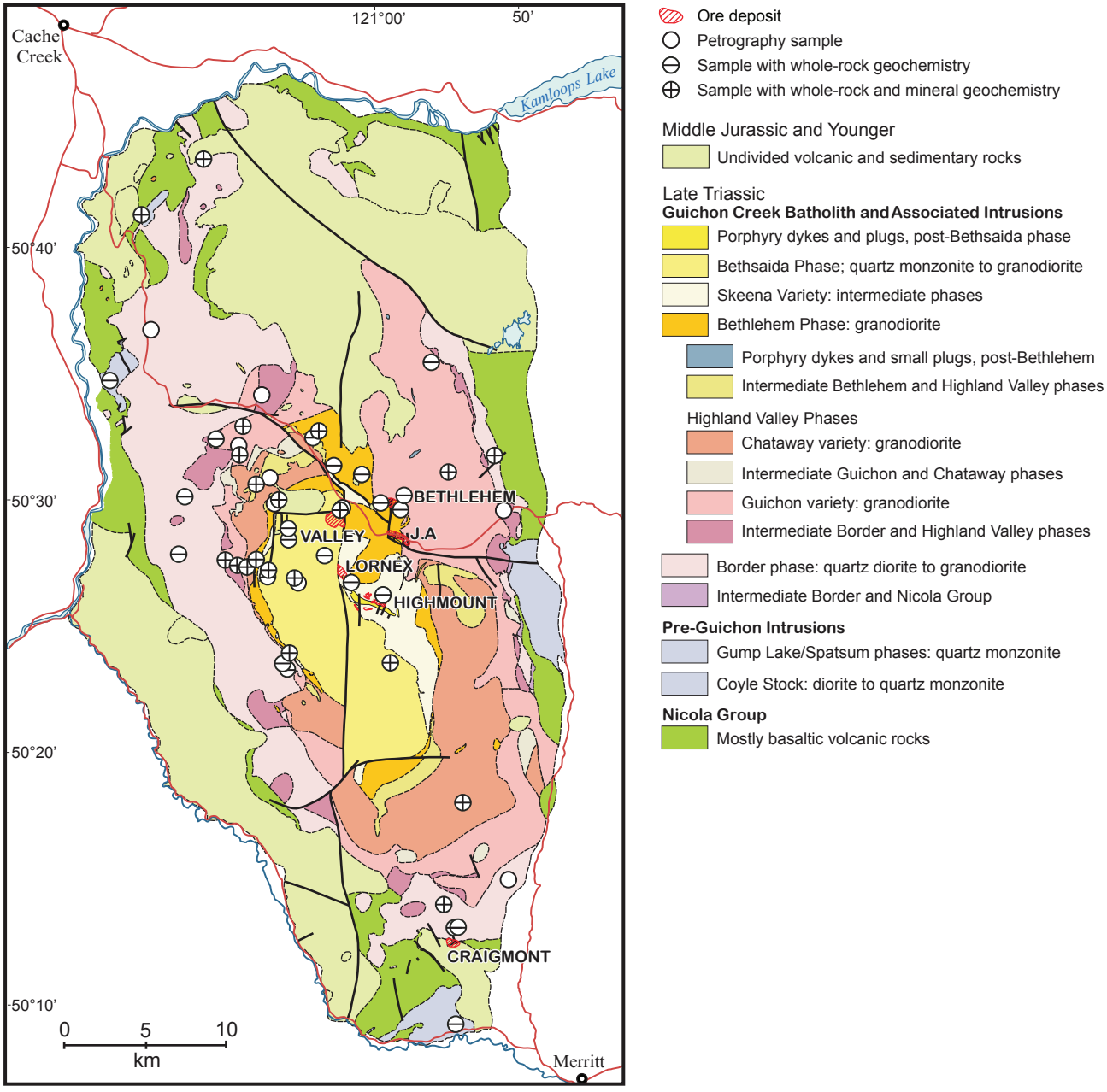

Figure 3: Simplified geology of the Guichon Creek batholith, showing the main intrusive phases and sample locations (summarized and redrafted after McMillan et al., 2009).

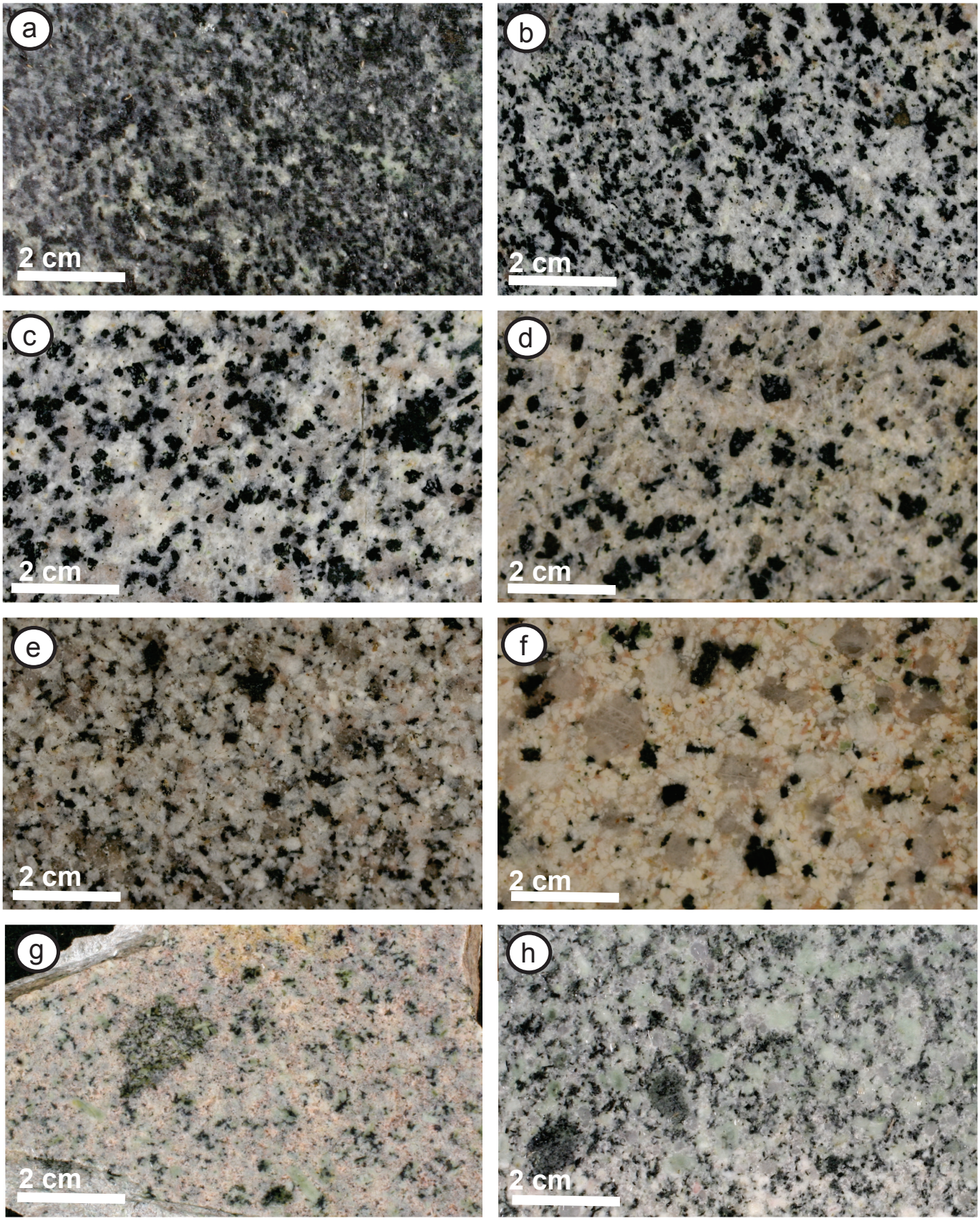

Figure 4: Representative samples of the main rocks at Guichon Creek batholith: (a) Border phase (sample# 15FbB-05), (b) Guichon (2238825), (c) Chataway (2238899), (d) Bethlehem (2238888), (e) Skeena (2238818), (f) Bethsaida (2238689), (g) Aplite dyke (15FB-13), (h) Spatsum 15FB-22).

Granite Mountain Batholith

The Late Triassic Granite Mountain batholith measures 18 x 10 km and occurs near McLeese Lake in south-central BC and hosts the Gibraltar porphyry Cu-Mo mine (Fig. 5). The batholith is subdivided into three main units, from southwest to northeast: Border phase diorite to quartz diorite, Mine phase tonalite and Granite Mountain phase leucocratic tonalite (Fig. 6). The Burgess Creek stock (Panteleyev, 1978), to the northeast, comprises a heterogeneous assemblage of tonalite, quartz diorite and diorite that intrudes the Nicola Group. Panteleyev (1978) considered the stock to be younger than the Granite Mountain batholith, but dating by Schiarizza (2015) shows that it is 4 to 5 m.y. older than the adjacent Granite Mountain phase of the batholith. As suggested by Ash et al. (1999), the Burgess Creek stock may represent the border phase part of the batholith. The Granite Mountain phase (217.2 ± 0.2 Ma, Schiarizza 2015) is slightly older than the Mine phase (216.2 ± 0.2, Mostaghimi, 2016).

Originally considered to intrude the Cache Creek terrane (Bysouth et al., 1995), mapping by Schiarizza (2015) convincingly shows Nicola Group strata on the northeastern margin of the Granite Mountain batholith, thus indicating it is part of the Quesnel terrane. Interpretations of aeromagnetic data confirm these observations (Sánchez et al., 2015). Thus, the Granite Mountain batholith is recognized as correlative with the Late Triassic, calc-alkaline Guichon Creek batholith, which hosts the

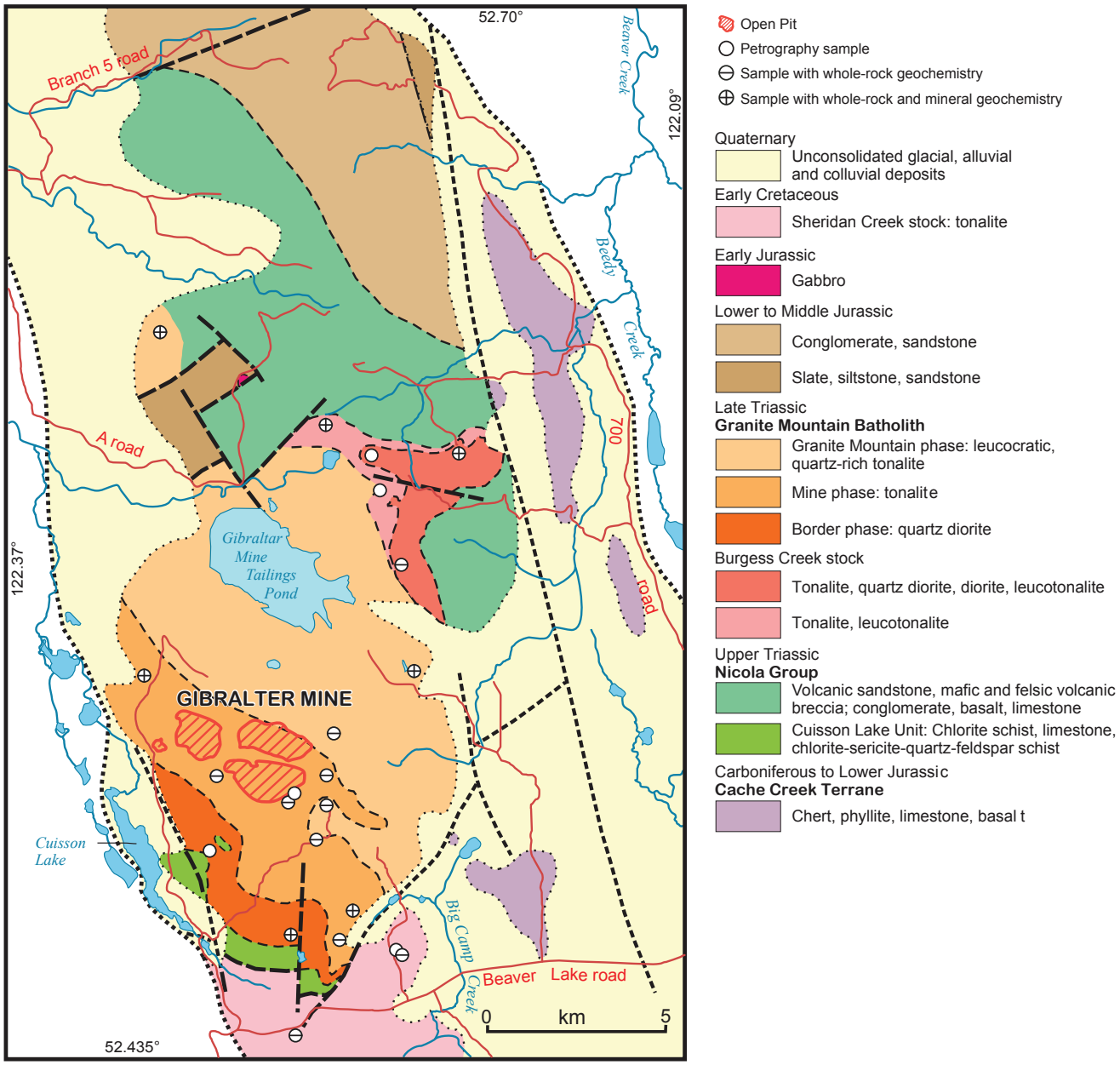

Figure 5: Geology of the Granite Mountain batholith, showing the main intrusive units and sample locations (after Schiarizza, 2015).

Highland Valley porphyry Cu-Mo deposits, 250 km to the south-southeast.

Mineralization at the Gibraltar mine is hosted in the Mine phase tonalite of the Granite Mountain batholith, but small porphyry-style mineral occurrences are also known in the Border phase and the Granite Mountain phase (Schiarizza, 2015). The Mine phase is commonly altered whereas the Border phase and the Granite Mountain phase are rarely altered. Moreover, the age of the mineralization (215 ± 1.0 to 210 ± 0.5 Ma) based on three Re-Os dates (Harding, 2012) indicates that the mineralization was penecontemporaneous with the emplacement of the Mine phase.

Takomkane Batholith

The Takomkane batholith (Fig. 7) is a large, 50 x 40 km Late Triassic–Early Jurassic composite batholith that hosts several mineralized porphyry centres. It intrudes the Late Triassic Spout Lake pluton and is cut by Early Jurassic ultramafic–mafic plutons and the Early Cretaceous Boss Mountain Mine stock. The Takomkane batholith consists of two major units: the Late Triassic–Early Jurassic Boss Creek unit and the Early Jurassic megacrystic Schoolhouse Lake unit. Thus, the Boss Creek is the older phase of the batholith dated between 202.5 ± 0.5 to 199.5 ± 0.3 Ma (two zircon U/Pb ages) and the Schoolhouse Lake unit is the younger phase of the batholith dated between 195.0 ±

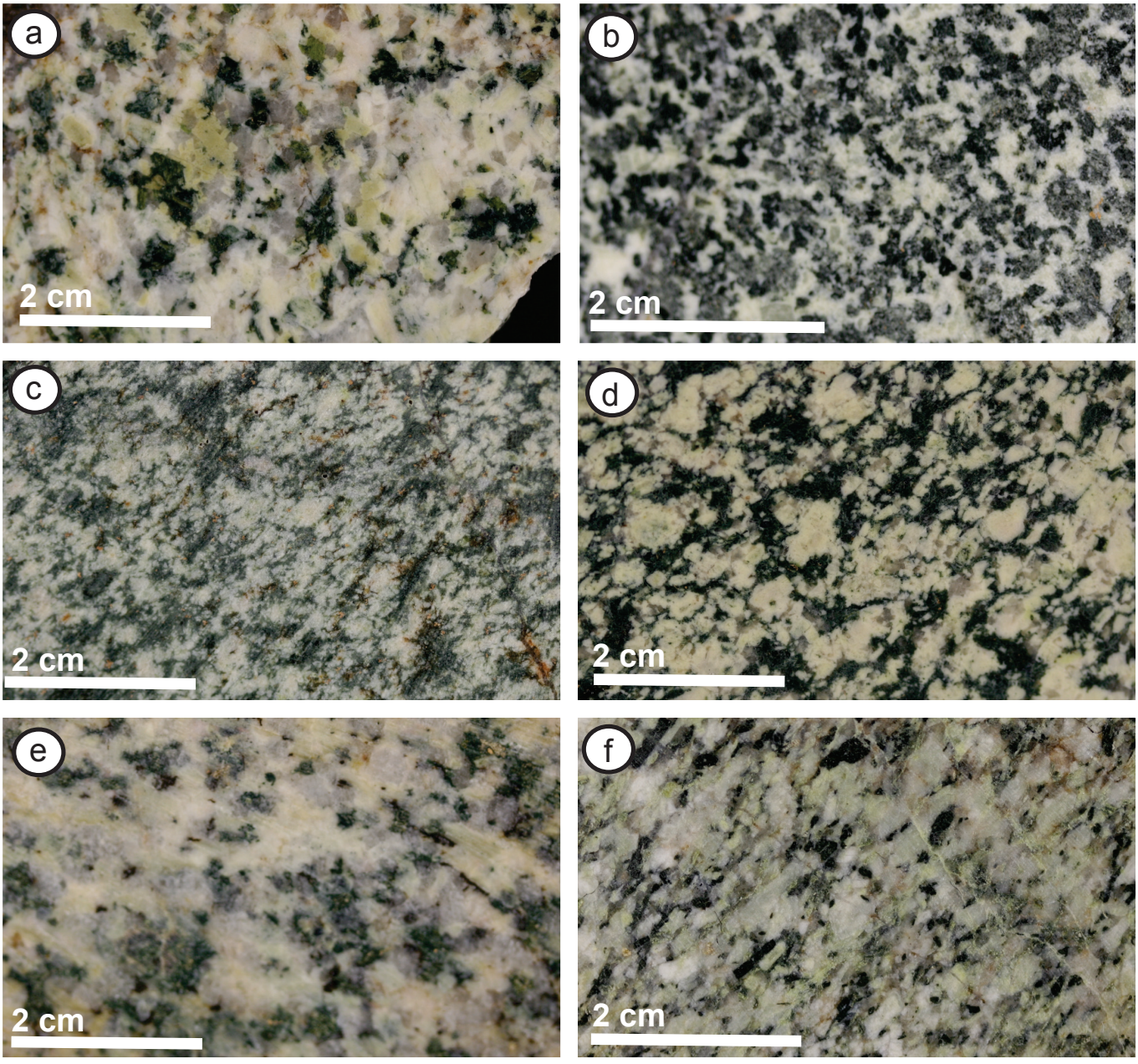

Figure 6: Representative samples of the main rocks at Granite Mountain batholith: (a) Burgess (13PSC-150), (b) Burgess Mixed (13PSC-100), (c) Border phase (14PSC-171), (d) Mine phase (14PSC-380), (e) Granite Mountain phase (14PSC-335), (f) Sheridan stock (14PSC-374).

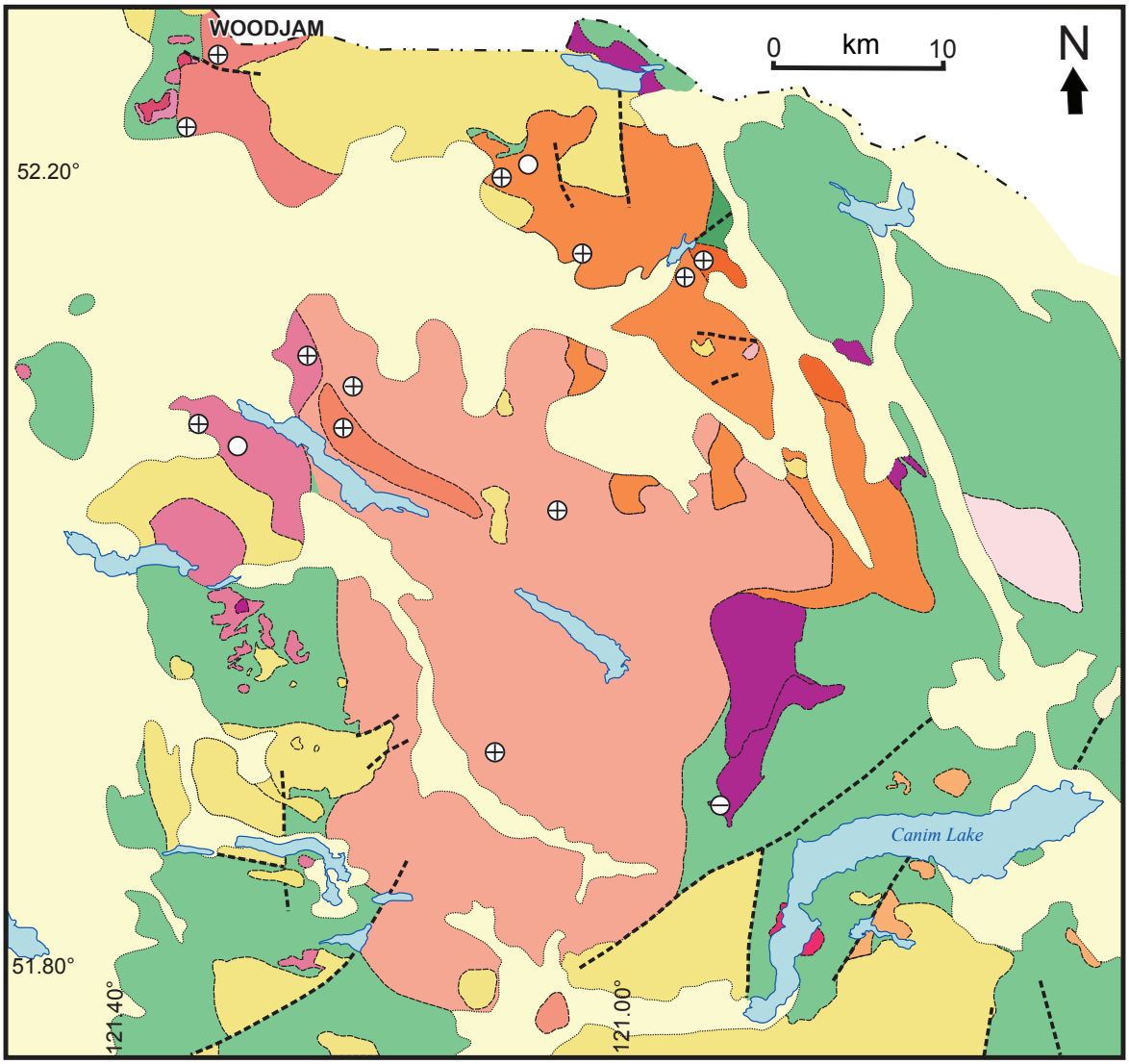

Figure 7: Simplified geology of the Takomkane batholith, showing the main intrusive units and sample locations (after Schiarizza et al., 2013).

0.4 to 193.5 ± 0.6 Ma (Schiarizza et al., 2009). A smaller-volume unit of quartz-feldspar porphyry occurs within the Schoolhouse Lake unit. The Woodjam Creek unit is texturally distinct but compositionally similar to the Schoolhouse Lake unit and forms the northwestern part of the batholith (Schiarizza et al., 2009). The Woodjam Creek unit (194.99 ± 0.16 Ma, del Real et al., 2017) has a similar age to the Schoolhouse Lake unit but has less quartz and does not contain the large K-feldspar megacrysts that characterize the latter (Fig. 8).

Several small Cu showings occur within the Spout Lake pluton and, to a lesser extent, within the Boss Creek and Schoolhouse units (Schiarizza et al., 2009). Mineralization at the Spout Lake pluton consists of those described at Celo, Bory, Murphy Lake, SL, Rover, and Harrison Creek (Schiarizza et al., 2009). These are mostly chalcopyrite, pyrite and locally bornite and magnetite veins. Similar mineralization occurs with the Boss Creek pluton at Rodeo and Luky Jack prospects. Mineralization with the Schoolhouse Lake pluton occurs at the Granite Mountain prospect in the central parts of the batholith which is characterized by chalcopyrite and pyrite occurring in shear zone hosted quartz veins suggesting a significantly deeper setting for the mineralization. Economically the most significant Cu-Mo-Au porphyry mineralization, however, occurs along the northwestern boundary of the batholith in the Woodjam area (Southeast Zone, Deerhorn and Takom deposits). These deposits are hosted within a largely equigranular quartz monzonite unit, for example at Southeast Zone, or in small porphyry dikes and

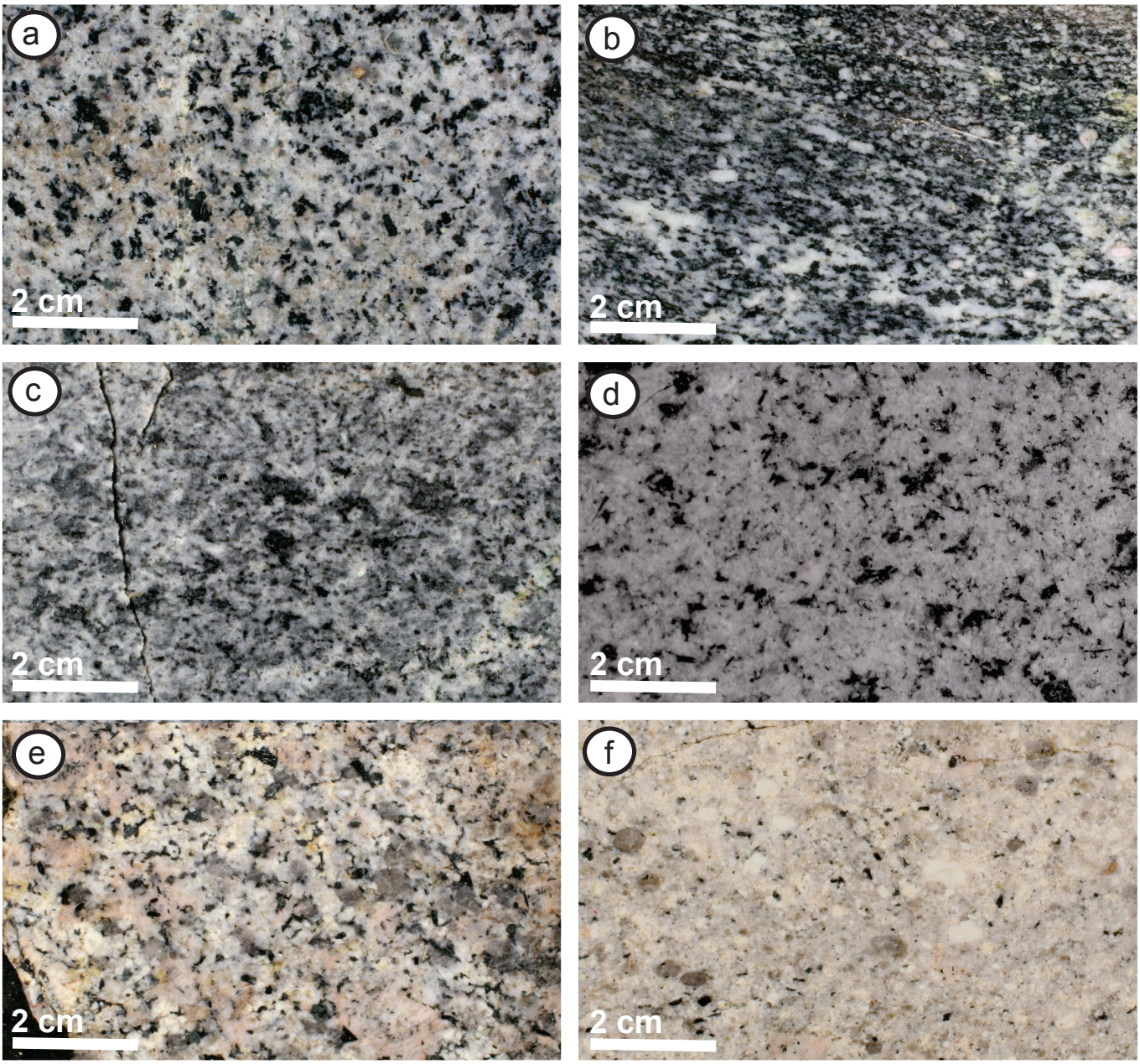

Figure 8: Representative samples of the main rocks at Takomkane batholith: (a) Spout Lake (15FB-28), (b) Buster Lake (15FB-33), (c) Boss Creek (15FB-34), (d) Woodjam Creek (11FB-01), (e) Schoolhouse Lake (15FB-36), (f) Quartz Feldspar Porphyry (15FB-35).

in adjacent volcanic rocks, for example at Deerhorn (del Real et al., 2017). Age relationships demonstrate that the Southeast zone (197.48 ± 0.33 Ma), Takom (197.16 ± 0.15 Ma), and Deerhorn (196.34 ± 0.19 Ma) intrusions were emplaced over approximately 1 m.y. as spatially discrete intrusive events (del Real et al., 2017) just prior to emplacement of the Woodjam and Schoolhouse units. The proximity of the Woodjam Creek unit at the margin of the batholith to these mineralized centers as well as its close age, textural and geochemical similarities suggests that Woodjam Creek unit probably represents deeper intrusive stock for the mineralization at the Woodjam area (del Real et al., 2017).

SAMPLES AND METHODS

Rock samples were collected from various intrusive phases of the Guichon Creek, Takomkane and Granite Mountain batholiths. In total, 110 rock samples were collected: 53 from Guichon Creek, 31 from Takomkane and 26 from Granite Mountain. Sample locations are shown in Figures 3, 5 and 7. Hand sawn samples were described and further characterized with microscope petrographic studies. A sub-set of samples representing fresh main intrusive bodies were selected, including: 27 from Guichon Creek, 23 from Takomkane and 10 from Granite Mountain batholith. The altered host rocks were avoided in order not to mix the fertility characteristics with those of the alteration effects.

Samples were disaggregated using an electric-pulse disaggregator (EPD) at Overburden Drilling Management Limited (Nepean, Ontario) to break the rock along mineral-grain boundaries, thus providing a larger number of unbroken mineral grains. Subsequently, mineral separation was performed at MDRU - Mineral Deposit Research Unit, The University of British Columbia using Frantz® magnetic separation and conventional heavy liquid methods.

Mineral grains were handpicked, mounted and polished in preparation for electron-probe microanalysis (EPMA) and trace-element laser-ablation inductively coupled plasma–mass spectrometry (LA-ICP-MS) at The University of British Columbia. A total of 581 apatite grain and 689 titanite grains were mounted and analyzed. These grains were studied and characterized by binocular, petrographic and cathodoluminescence (CL) microscopy, as well as by scanning electron microscope (SEM). Properties such as colour, shape, inclusion populations, zoning and replacements were documented for each grain. Mineral grains were then analyzed by EPMA for major elements and some trace elements. Subsequently, the same grains and spots were analyzed by LA-ICP-MS for a full trace-element characterization. For smaller grains (<100 microns) one spot was analyzed per sample. For larger grains (>100 microns), and where zoning is evident, two spots were analyzed per grain: one at the grain center and one at the rim.

Analytical Methods

Whole-rock samples were analyzed for major and trace elements at Bureau Veritas Minerals (Vancouver, BC) using research grade methods of Lithium Borate Fusion (LF700 and LF100) and Aqua Regia ICP-ES/MS (AQ200) to characterize the geochemical signature of each intrusive unit and to compare the mineral chemistry with whole-rock chemistry.

A Cambridge Image Technology Ltd MK 4A model cold cathodoluminescence (CL) stage mounted on a petrographic microscope was used to study the internal textures of the apatite grains. The samples were irradiated in a vacuum chamber with an electron beam of approximately 15 kV and the current set at 350–500 µA. Petrographic studies of apatite grains under transmitted light, and CL were used to select areas free of inclusions for analysis. Textural properties of titanite grains were studied under Scanning Electron Microscope (SEM).

Electron-probe microanalyses of apatite and titanite were conducted using a fully automated CAMECA SX-50 instrument, operating in the wavelength-dispersion mode. The operating conditions for apatite were as follow: excitation voltage, 15 kV; beam current, 10 nA; peak count time, 20 s (40 s for F, Cl); background count-time, 10 s (20 s for Cl); spot diameter of 10 µm for improved detection of more volatile elements or elements thought to be affected by diffusion processes such as F, Cl and Na (Stormer et al., 1993). For the elements considered, the following standards, X-ray lines and crystals were used: albite, Na$K\alpha$, TAP; kyanite, Al$K\alpha$, TAP; diopside, Mg$K\alpha$, TAP; apatite, P$K\alpha$, TAP; apatite, Ca$K\alpha$, PET; barite, S$K\alpha$, PET; synthetic rhodonite, Mn$K\alpha$, LIF; $SrTiO_3$, Sr$L\alpha$, TAP; topas, F$K\alpha$, TAP; scapolite, Cl$K\alpha$, PET. Data reduction involved the 'PAP' $\phi(\rho Z)$ method (Pouchou and Pichoir 1985). The operating conditions for titanite were as follow: excitation voltage, 15 kV; beam current, 20 nA; peak count time, 20 s; background count-time, 10 s; spot diameter, 5 µm. Data reduction was done using the 'PAP' $\phi(\rho Z)$ method (Pouchou & Pichoir 1985). For the elements considered, the following standards, X-ray lines and crystals were used: albite, Na$K\alpha$, TAP; diopside, Mg$K\alpha$, TAP; kyanite, Al$K\alpha$, TAP; diopside, Si$K\alpha$, TAP; diopside, Ca$K\alpha$, PET; rutile, Ti$K\alpha$, LIF; V element, V$K\alpha$, LIF; synthetic rhodonite, Mn$K\alpha$, LIF; synthetic fayalite, Fe$K\alpha$, LIF.

Three standard deviations (99.7% confidence level) were used for the calculation of detection limits. Analyses with values below 99.7% confidence level are assumed to be part of background and are not reported. These values however are displayed graphically to show the relative concentrations in various types of grains. Apatite formulae were calculated on the basis of five atoms of Al, Ce, Fe, Mn, Mg, Ca, Na. We assumed that Si and S substitute for P (Elliot, 1994). Titanite stoichiometries were calculated assuming five equivalent oxygen atoms per formula unit. Stoichiometry and total values were used to determine acceptance of each analyses. In total, 881 spots of apatite and 1076 spots of titanite were analyzed.

LA-ICP-MS analyses were carried out using a Resonetics m50-LR 193 nm excimer laser coupled to an Agilent 7700x ICP-MS with laser diameter of approximately 34 µm. Ablation time was 40 s with He gas flow (750 ml/min He and 2ml/min N_2). Thirty-five masses were analyzed for apatite and 36 masses for titanite in this study, including ^{43}Ca and ^{49}Ti as the internal standard for apatite and titanite, respectively, using the concentrations obtained by EPMA. Glitter 4.0 software was used to determine elemental concentrations using a NIST SRM 612 glass standard for external standardization. Intervals for data reduction were chosen based on the flattest part of the ^{43}Ca plateau (for apatite) or ^{49}Ti (for titanite), typically ~ 2 seconds after the laser turned on and around 2 seconds before the laser was turned off. During the data reduction a careful check on the multi-element mass spectra eliminated any possible impurities that may have been encountered across the depth profile of each laser-ablated area by assessing the ^{43}Ca or ^{49}Ti profile and inspecting for depressions, and examining for spikes of other masses that indicated the presence of inclusions. In total, 56 apatite and 98 titanite spots analyzed were rejected. The precision and accuracy of the analyses undertaken during this study are better than ±10%.

Tables 1, 2 and 3 provide results of chemical analyses of representative rock and grains from each pluton.

WHOLE ROCK GEOCHEMISTRY

Representative samples were analyzed for whole rock geochemistry from Guichon Creek (42 samples), Takomkane (15 samples) and Granite Mountain (26 samples) batholiths. Field characterization and loss on ignition were used to distinguish altered samples. All samples were fresh or weakly altered except two samples from the Skeena (2238872 and 2238875) and one sample of the Bethsaida phase (09FB-05) of the Guichon Creek batholith which showed high LOI (> 4%) and low Na_2O. Samples were also screened for positive europium anomalies where Eu/Eu*>1.3 suggests plagioclase fractionation and extraction as cumulates as described by Loucks (2014). One sample (14PSC-171 from the Granite Mountain Border phase) displayed a europium anomaly of 1.46 and it was cautiously kept in the database.

Major Elements

Guichon Creek rocks range in composition from gabbroic diorite to diorite at the border phase to largely granodiorite for the Bethlehem, Skeena and Bethsaida phases (Fig. 9) which occur in the central parts of the batholith. The Guichon and Chataway phases have compositions of diorite and granodiorite. Late aplite dikes have granitic composition. One analyzed sample of the Coyle stock (post-Nicola) has a granite composition (Table 1).

From Takomkane, samples of the Late Triassic Spout Lake pluton have monzonite to quartz monzonite compositions. The Late

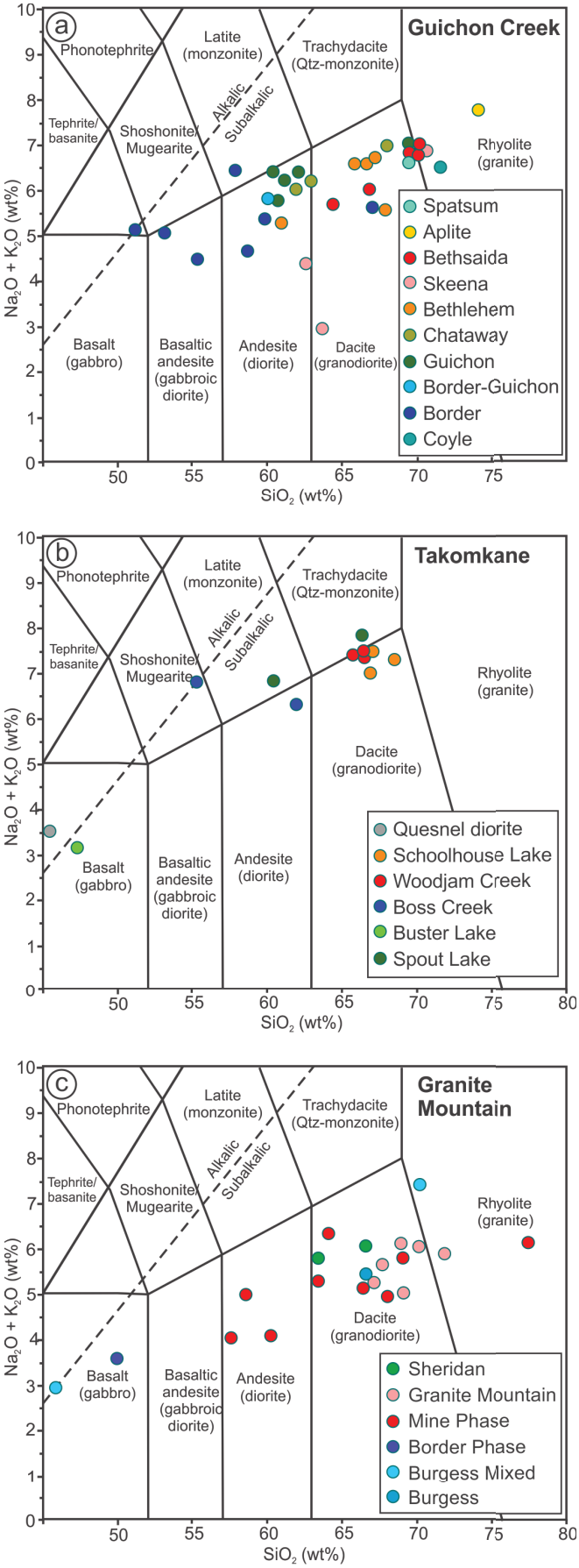

Figure 9: Total alkali-silica (TAS) diagram of Guichon Creek, Takomkane and Granite Mountain batholiths.

Table 1: Representative whole rock analysis of Guichon Creek, Granite Mountain and Takomkane plutonic suites

Sample #	Method	Unit	Detection Limit	15FB-01	2238923	15FB-17	2238899	09FB-02	2238872	2238767	15FB-13	15FB-22
Batholith				Guichon Creek								
Unit				Coyle	Border Phase	Guichon Variety	Chataway Variety	Bethlehem Phase	Skeena Variety	Bethsaida Phase	Aplite dyke	Spatsum
Lithology				granite	diorite	diorite	granodiorite	granodiorite	granodiorite	granodiorite	aplite	granodiorite
Lat (WGS 84)				50.1550	50.5273	50.5150	50.5080	50.4936	50.4322	50.4695	50.6858	50.5772
Long				-120.9103	-121.1545	-120.9296	-121.1359	-121.0010	-121.0003	-121.1008	-121.2404	-121.2797
SiO_2	LF700	%	0.1	71.6	57.9	61	63	67.9	62.5	70.1	74.1	69.4
Al_2O_3	LF700	%	0.01	14.07	16.69	16.56	16.55	16.34	16.77	15.99	12.93	14.05
Fe_2O_3	LF700	%	0.01	2.72	6.96	5.46	4.7	2.46	1.94	1.85	3.28	3.73
CaO	LF700	%	0.01	2.21	5.01	5.49	5.05	3.96	5.36	2.96	0.9	2.34
MgO	LF700	%	0.01	0.8	3.14	3.06	2.35	1.15	0.45	0.51	0.29	1.3
Na_2O	LF700	%	0.01	4.11	3.97	4.1	4.29	5.18	3.08	5.1	4.35	4.51
K_2O	LF700	%	0.01	2.41	2.49	2.17	1.97	0.4	1.32	1.88	3.43	2.11
MnO	LF700	%	0.01	0.03	0.11	0.09	0.07	0.03	0.03	0.05	0.07	0.06
TiO_2	LF700	%	0.01	0.41	0.93	0.65	0.53	0.35	0.31	0.2	0.34	0.48
P_2O_5	LF700	%	0.01	0.1	0.2	0.16	0.15	0.13	0.13	0.07	0.05	0.09
Cr_2O_3	LF700	%	0.001	<0.001	0.002	0.003	<0.001	<0.001	0.002	<0.001	<0.001	0.002
Ba	LF700	%	0.01	0.08	0.1	0.07	0.09	0.03	0.08	0.1	0.1	0.05
LOI	LF700	%		1.44	1.99	0.9	0.87	1.64	7.65	0.57	0.56	1.2
Cu	LF700	%	0.01	<0.01	0.02	0.01	<0.01	0.05	0.1	<0.01	<0.01	<0.01
Ni	LF700	%	0.01	<0.01	<0.01	<0.01	<0.01	<0.01	<0.01	<0.01	<0.01	<0.01
Pb	LF700	%	0.01	<0.01	<0.01	<0.01	<0.01	<0.01	<0.01	<0.01	<0.01	<0.01
SO_3	LF700	%	0.002	0.011	0.005	0.002	0.003	0.006	0.113	0.003	0.005	0.003
Sr	LF700	%	0.002	0.015	0.048	0.057	0.061	0.082	0.045	0.061	0.016	0.022
V_2O_5	LF700	%	0.002	0.007	0.032	0.027	0.023	0.012	0.009	0.006	0.002	0.012
Zr	LF700	%	0.002	0.01	0.014	0.011	0.012	0.009	0.004	0.004	0.023	0.015
Total	LF700	%	0.01	100.03	99.63	99.9	99.8	99.81	99.94	99.51	100.51	99.38
Total/C	TC000	%	0.02	0.09	0.03	<0.02	<0.02	<0.02	1.3	0.36	<0.02	0.04
Total/S	TC000	%	0.02	<0.02	<0.02	<0.02	<0.02	<0.02	0.05	<0.02	<0.02	<0.02
Ba	LF100	ppm	1	809	1083	714	978	340	729	1100	1064	529
Be	LF100	ppm	1	<1	<1	<1	<1	2	<1	<1	<1	2
Co	LF100	ppm	0.2	2.5	23	16.7	14.7	9.4	2.9	2.8	2	6.7
Cs	LF100	ppm	0.1	0.5	1.6	1.7	1	0.3	1.4	0.9	1.1	2.2
Ga	LF100	ppm	0.5	12.4	20.7	17.3	20.3	20.4	16.8	16.6	12.8	12.8
Hf	LF100	ppm	0.1	3.7	5.1	3.7	4.8	2.8	1.6	2.2	9.2	5.6
Nb	LF100	ppm	0.1	4.3	4.8	2.9	2.3	3.6	1.6	1.5	4.5	2.4
Rb	LF100	ppm	0.1	44.9	66.2	62.3	46.3	8.7	20.9	29.4	78.4	37.9
Sn	LF100	ppm	1	2	<1	<1	<1	<1	<1	<1	2	<1
Sr	LF100	ppm	0.5	227.6	677	657.2	768.7	1091.4	528.7	725.3	155.6	210.6
Ta	LF100	ppm	0.1	0.4	0.3	0.2	<0.1	0.3	0.1	0.1	0.3	0.1
Th	LF100	ppm	0.2	4.2	3.5	5	2.5	3.5	1.7	1.1	5.7	3.1
U	LF100	ppm	0.1	1.4	1.6	2.3	1.2	3.1	0.7	0.6	3.6	2
V	LF100	ppm	8	39	208	145	140	80	50	34	<8	55
W	LF100	ppm	0.5	0.6	1.3	0.5	<0.5	0.6	13.6	<0.5	0.7	0.8
Zr	LF100	ppm	0.1	153.2	210.5	130.2	190.9	108.7	46.3	86.8	293.8	179.3
Y	LF100	ppm	0.1	16.7	19.1	14.1	11.4	10.5	5	4.8	49.6	29
La	LF100	ppm	0.1	15.8	18.2	14.7	13.6	13.9	9.4	9.8	18.1	9.5
Ce	LF100	ppm	0.1	27	37.6	33.9	28.3	32.4	17.7	17.7	43.4	23.1
Pr	LF100	ppm	0.02	3	4.84	4.11	3.5	4.27	2.29	1.95	6.04	3.2
Nd	LF100	ppm	0.3	11.4	21.8	17.7	14.6	16.2	8.2	7	26.7	14.9
Sm	LF100	ppm	0.05	2.3	4.6	3.28	2.9	3.08	1.48	1.16	6.77	3.93
Eu	LF100	ppm	0.02	0.72	1.15	0.91	0.77	0.79	0.51	0.41	1.39	0.83
Gd	LF100	ppm	0.05	2.57	3.94	3.03	2.36	2.24	1.28	0.96	7.81	4.22
Tb	LF100	ppm	0.01	0.4	0.58	0.41	0.36	0.31	0.17	0.14	1.25	0.74
Dy	LF100	ppm	0.05	2.82	3.43	2.52	1.82	1.8	0.87	0.87	8.7	4.7
Ho	LF100	ppm	0.02	0.58	0.68	0.48	0.41	0.33	0.19	0.14	1.74	0.98
Er	LF100	ppm	0.03	1.89	2.01	1.52	1.19	0.96	0.5	0.54	5.43	3.11
Tm	LF100	ppm	0.01	0.3	0.27	0.21	0.15	0.14	0.07	0.08	0.82	0.46
Yb	LF100	ppm	0.05	2.13	1.91	1.43	1.13	1.08	0.47	0.65	5.81	3.25
Lu	LF100	ppm	0.01	0.34	0.29	0.22	0.18	0.17	0.08	0.11	0.89	0.5
Mo	AQ200	ppm	0.1	0.7	1.1	0.7	0.5	16	15.9	<0.1	0.9	0.7
Cu	AQ200	ppm	0.1	7.7	191.1	145.5	26.4	565.1	1001	4.6	17.6	5.2
Pb	AQ200	ppm	0.1	5.2	1.8	1.9	0.6	0.6	2.4	2.1	3.2	1.3
Zn	AQ200	ppm	1	15	67	34	25	13	15	29	20	12
Ni	AQ200	ppm	0.1	2.1	16.8	16	8.6	5.7	1	0.8	0.4	3.3
As	AQ200	ppm	0.5	2	3.5	0.6	<0.5	1.9	105.7	<0.5	1	2.7
Sb	AQ200	ppm	0.1	<0.1	0.3	<0.1	<0.1	0.2	<0.1	<0.1	<0.1	0.5
Ag	AQ200	ppm	0.1	<0.1	<0.1	<0.1	<0.1	<0.1	0.5	<0.1	<0.1	<0.1
Au	AQ200	ppb	0.5	1.3	3.1	2.3	2.6	2	1.1	1.7	<0.5	<0.5

Table 1: (cont.)

Sample #	13PSC-144	13PSC-100	14PSC-171	14PSC-386	14PSC-335	15FB-42	15FB-26	15FB-33	15FB-34	11FB-01	15FB-38	15FB-39
Batholith	Granite Mountain						Takomkane					
Unit	Burgess Creek	Burgess Creek mixed	Border Phase	Mine phase	Granite Mountain Phase	Sheridan Creek	Spout Lake	Buster Lake	Boss Creek	Woodjam Creek	Schollhouse Lake	Quesnel Diorite
Lithology	granodiorite	diorite	diorite	granodiorite	granodiorite	granodiorite	quartz monzonite	gabbro	diorite	quartz monzonite	granodiorite	gabbro
Lat (WGS 84)	52.5949	52.5627	52.4673	52.5342	52.5178	52.4586	52.0603	52.1514	52.1461	52.2575	51.9098	51.8768
Long	-122.2356	-122.2073	-122.2530	-122.3153	-122.2352	-122.2087	-121.3527	-120.9386	-120.9509	-121.3420	-121.0956	-120.9295
SiO_2	66.6	46	50	63.3	68.9	63.4	66.4	47.3	55.3	66.7	68.6	44.6
Al_2O_3	15.92	18.07	19.61	15.66	15.35	16.4	16.13	24.29	20.58	16.21	15.25	12.06
Fe_2O_3	3.5	8.86	8.26	4.63	2.72	4.23	3.05	6.38	5.9	3.52	2.96	12.78
CaO	4.07	11.26	8.56	4.66	3.43	4.94	3.17	12.96	7.01	3.98	3.19	10.82
MgO	1.43	7.5	5.17	2.28	0.99	2.39	1.14	3.62	1.79	1.17	0.97	9.83
Na_2O	4.89	2.12	3.47	4.16	4.65	4.55	4.19	2.38	3.87	4.02	4.26	2.43
K_2O	0.49	0.76	0.12	1.13	1.47	1.21	3.73	0.82	3	3.42	3.1	1.07
MnO	0.08	0.17	0.2	0.12	0.06	0.06	0.05	0.13	0.11	0.04	0.08	0.17
TiO_2	0.36	0.76	0.81	0.46	0.25	0.59	0.22	0.37	0.66	0.34	0.29	1.21
P_2O_5	0.09	0.09	0.13	0.11	0.08	0.24	0.11	0.06	0.37	0.13	0.13	0.41
Cr_2O_3	<0.001	0.02	0.004	<0.001	<0.001	0.004	<0.001	0.002	<0.001	<0.001	<0.001	0.048
Ba	0.04	0.05	<0.01	0.06	0.07	0.08	0.13	0.04	0.27	0.18	0.11	0.04
LOI	1.96	3.67	3.2	2.8	2.98	1.59	1	1.66	0.72	0.46	0.8	3.01
Cu	<0.01	<0.01	<0.01	<0.01	<0.01	<0.01	<0.01	<0.01	0.02	0.02	<0.01	<0.01
Ni	<0.01	<0.01	<0.01	<0.01	<0.01	<0.01	<0.01	<0.01	<0.01	<0.01	<0.01	0.01
Pb	<0.01	<0.01	<0.01	<0.01	<0.01	<0.01	<0.01	<0.01	<0.01	<0.01	<0.01	<0.01
SO_3	0.003	0.005	0.012	0.007	0.003	0.005	0.023	0.019	0.007	0.007	0.019	0.871
Sr	0.046	0.029	0.039	0.032	0.031	0.062	0.052	0.075	0.064	0.046	0.051	0.035
V_2O_5	0.01	0.044	0.042	0.022	0.007	0.014	0.011	0.035	0.031	0.014	0.011	0.08
Zr	0.013	<0.002	<0.002	0.011	0.007	0.007	0.007	<0.002	0.007	0.005	0.005	<0.002
Total	99.56	99.47	99.67	99.5	101	99.76	99.46	100.18	99.74	100.36	99.82	99.53
Total/C	0.1	0.21	0.02	0.21	0.39	0.05	0.05	0.04	<0.02	<0.02	0.07	0.49
Total/S	<0.02	<0.02	<0.02	<0.02	<0.02	<0.02	<0.02	<0.02	<0.02	0.02	<0.02	0.73
Ba	421	505	88	601	722	809	1306	386	2613	1742	1168	402
Be	3	2	2	<1	<1	1	1	<1	1	2	<1	<1
Co	7.2	34	24.2	10.7	4.2	11	4.8	14	11.4	3.6	4.8	40.1
Cs	0.4	0.2	0.1	0.4	0.6	0.5	1.6	1.7	0.6	1.1	2.1	0.4
Ga	16.8	15.9	19.4	16.7	15.1	15.4	13.7	18.6	17.4	15.5	14	13.5
Hf	2.6	0.6	0.5	4.1	2.6	3	2.9	0.8	3.1	2.9	2.2	1.5
Nb	1.7	0.8	0.8	2.1	2	9.3	2.6	0.7	2.3	1.9	1.6	1.3
Rb	6.6	11.3	1.6	19.7	20.7	18.5	81	13.5	38.3	62.6	83.4	15.9
Sn	<1	<1	<1	<1	<1	<1	<1	3	<1	<1	<1	<1
Sr	495.4	406.6	506.1	421.9	342	712.4	566.9	882.5	650.2	574.2	592.5	454.3
Ta	0.1	<0.1	<0.1	<0.1	0.2	0.7	0.3	0.1	0.1	0.2	0.2	0.1
Th	0.8	<0.2	<0.2	1.4	1.1	3.4	4.2	0.3	0.2	4.4	3.7	0.6
U	0.3	<0.1	<0.1	0.9	0.5	1.6	2.4	0.1	0.3	2.6	3.1	0.6
V	68	245	233	116	44	77	58	161	136	65	53	421
W	<0.5	<0.5	<0.5	<0.5	<0.5	1.2	<0.5	<0.5	<0.5	<0.5	<0.5	1.8
Zr	93.9	17.5	16.3	145.4	81.5	115	96.6	18.9	111.2	99.5	67.1	43.2
Y	10.8	11	8.8	15.4	9.9	8	10.9	11.7	15.2	9	7.6	20.5
La	6.4	1.9	2.5	8.7	4.7	16.1	9.7	3.9	9.4	9.5	9.3	5.6
Ce	14.5	5.4	5.5	19.5	12	31.9	16.6	8	20	16.7	16.4	13.4
Pr	1.87	0.94	0.81	2.54	1.69	3.68	1.95	1.23	2.65	1.95	1.86	2.2
Nd	8.9	5.5	4.4	11.8	7.9	14.5	7.4	5.8	12.2	8.2	7.7	11.5
Sm	1.91	1.64	1.27	2.65	1.69	2.66	1.61	1.53	2.73	1.54	1.5	3.31
Eu	0.54	0.64	0.69	0.66	0.49	0.85	0.51	0.65	0.82	0.5	0.41	0.97
Gd	2.02	2.23	1.64	2.71	1.77	2.19	1.56	1.79	2.89	1.57	1.38	3.78
Tb	0.29	0.36	0.26	0.41	0.27	0.3	0.26	0.31	0.46	0.25	0.21	0.59
Dy	1.83	2.14	1.74	2.55	1.62	1.7	1.58	1.91	2.63	1.47	1.23	3.83
Ho	0.37	0.49	0.33	0.5	0.33	0.3	0.36	0.39	0.55	0.33	0.26	0.79
Er	1.14	1.17	0.92	1.75	1.09	0.89	1.12	1.16	1.64	1.02	0.88	2.19
Tm	0.18	0.18	0.14	0.25	0.15	0.13	0.18	0.19	0.26	0.15	0.13	0.3
Yb	1.25	1.25	0.84	1.72	1.16	0.84	1.47	1.23	1.64	1.13	0.94	1.93
Lu	0.17	0.18	0.14	0.27	0.22	0.11	0.23	0.18	0.26	0.19	0.16	0.27
Mo	<0.1	<0.1	<0.1	0.2	<0.1	<0.1	0.4	<0.1	0.5	0.3	<0.1	<0.1
Cu	2.5	23.7	50	46	2.8	18.4	4.7	5.4	173.9	248.6	1.8	14.5
Pb	0.5	0.7	0.3	0.7	1	2.8	1.2	1.4	2.4	3.1	1.1	0.6
Zn	48	31	73	46	26	35	4	29	44	9	22	33
Ni	2.9	39.9	22.9	5.1	1.7	17.5	1.5	2.3	7.1	1	1.6	57.8
As	<0.5	0.6	0.6	<0.5	<0.5	<0.5	2.5	0.8	0.5	2.5	1.2	<0.5
Sb	<0.1	<0.1	<0.1	<0.1	<0.1	<0.1	<0.1	<0.1	<0.1	0.3	<0.1	<0.1
Ag	<0.1	<0.1	<0.1	<0.1	<0.1	<0.1	<0.1	<0.1	<0.1	<0.1	<0.1	<0.1
Au	0.7	0.6	<0.5	<0.5	<0.5	<0.5	<0.5	<0.5	2.8	<0.5	<0.5	4.6

Table 2: Representative analyses of apatite from the Guichon Creek, Granite Mountain and Takomkane batholiths.

Batholith	Detection limit	Guichon Creek							Granite Mountain		
Unit		Border	Guichon	Chataway	Bethlehem	Skeena	Bethsaida	Aplite	Burgess Creek	Burgess mixed	Granite Mountain
Rock		qtz-diorite	granodiorite	granodiorite	granodiorite	granodiorite	granodiorite	aplite	tonalite	tonalite	tonalite
CL Color		brown		dark brown	brown	brown	greenish brown		brown	dark green	brown
Sample#		15FB-05	15FB-07	2238899	15FB-19	2238818	09FB-04	15FB-13	13PSC-144	15FB-40	15FB-41
Analysis#		P20-07a-3	P23-02-5-4	P10-10-16-1	P20-04-15	P11-02-5	P10-07-16	P18-05b-4-3	P10-11a-1	P03-11-15	P10-02-7
Electorn-probe microanalysis (wt.%):											
Na_2O	0.05 (%)	0.11	0.10	0.06	0.07	0.04	0.10	0.05	0.09	0.25	0.06
MgO	0.06	0.05	0.03	0.03	0.03	0.02	0.01	0.02	<DL	0.06	0.03
Al_2O_3	0.08	0.02	<DL	<DL	0.01	<DL	<DL	0.02	<DL	0.01	0.01
SiO_2	0.13	0.19	0.28	0.18	0.30	0.06	0.06	0.24	0.12	0.29	0.19
P_2O_5	0.27	40.96	40.93	41.32	40.65	42.51	42.16	41.53	41.71	42.04	41.55
SO_3	0.17	0.20	0.46	0.23	0.33	0.26	0.12	0.19	0.09	0.19	0.25
CaO	0.09	53.71	55.50	55.18	55.51	56.13	54.46	55.11	55.72	54.58	56.07
MnO	0.15	0.21	0.13	0.02	0.03	0.13	0.88	0.06	0.21	0.12	0.06
FeO	0.21	0.26	0.07	0.05	0.04	0.00	0.06	0.02	0.06	0.22	0.04
Ce_2O_3	0.23	0.29	0.26	0.21	0.14	0.21	0.01	0.12	0.20	0.60	0.24
Cl	0.02	2.30	0.60	0.39	0.14	0.18	0.07	0.14	0.36	0.56	0.10
Total		98.30	98.36	97.68	97.25	99.54	97.93	97.48	98.55	98.93	98.60
Atomic formulae calculation (per formula unit):											
Na^{+}		0.018	0.017	0.010	0.012	0.007	0.016	0.008	0.015	0.041	0.010
Mg^{2+}		0.007	0.004	0.004	0.003	0.002	0.001	0.002	<DL	0.007	0.003
Al^{3+}		0.002	<DL	<DL	0.001	<DL	<DL	0.002	<DL	0.001	0.001
Ca^{2+}		4.931	4.957	4.975	4.974	4.976	4.916	4.979	4.960	4.908	4.971
Mn^{2+}		0.015	0.009	0.002	0.002	0.009	0.063	0.004	0.014	0.008	0.004
Fe^{2+}		0.019	0.005	0.003	0.003	0.000	0.004	0.001	0.004	0.016	0.003
Ce^{3+}		0.009	0.008	0.007	0.004	0.006	0.000	0.004	0.006	0.018	0.007
Subtotal		5.000	5.000	5.000	5.000	5.000	5.000	5.000	5.000	5.000	5.000
P^{5+}		2.971	2.888	2.944	2.879	2.978	3.007	2.965	2.934	2.988	2.911
Si^{4+}		0.016	0.023	0.016	0.025	0.005	0.005	0.020	0.010	0.025	0.016
S^{6+}		0.033	0.071	0.035	0.052	0.041	0.019	0.030	0.014	0.030	0.039
Subtotal		3.020	2.983	2.995	2.956	3.024	3.031	3.015	2.958	3.042	2.966
Cl^{-}		0.334	0.085	0.056	0.020	0.026	0.010	0.020	0.050	0.080	0.014
LA-ICP-MS microanalysis (ppm):											
^{23}Na	0.5 (ppm)	304.0	646.0	473.0	447.0	581.0	394.0	379.0	469.0	1108.0	614.0
^{27}Al	0.5	83.0	229.0	<DL	4.9	<DL	25.4	<DL	0.9	<DL	1.0
^{29}Si	0.5	1140.0	7200.0	270.0	1740.0	340.0	1610.0	800.0	790.0	1330.0	1830.0
^{30}Si	0.5	<DL	17300.0	<DL	4900.0	<DL	<DL	200.0	6500.0	200.0	9100.0
^{51}V	0.5	22.7	77.0	38.1	36.0	12.6	4.8	16.2	10.0	2.2	36.6
^{55}Mn	0.5	755.0	1046.0	746.0	593.0	1099.0	7210.0	901.0	669.0	81.5	835.0
^{63}Cu	0.5	73.0	36.0	0.5	1.6	<DL	0.6	7.5	0.5	10.7	1.3
^{88}Sr	0.5	366.0	360.5	395.0	270.3	245.3	371.6	260.7	178.3	16.5	153.4
^{89}Y	0.5	276.2	118.1	119.2	224.0	151.8	419.2	329.4	588.0	151.9	889.0
^{90}Zr	0.5	1.4	15.0	0.5	0.9	0.5	<DL	<DL	<DL	<DL	<DL
^{91}Zr	0.5	0.7	16.0	<DL	0.7	<DL	<DL	<DL	<DL	<DL	0.9
^{139}La	0.5	727.0	1132.0	1099.0	1069.0	574.3	279.0	509.3	526.0	123.2	788.0
^{140}Ce	0.5	1539.0	1681.0	1463.0	1391.0	757.0	885.0	1009.0	1400.0	329.4	2225.0
^{141}Pr	0.5	170.6	123.2	117.5	113.9	71.2	138.8	129.8	198.0	43.6	287.2
^{146}Nd	0.5	686.0	355.0	395.0	419.9	295.9	753.0	678.0	1013.0	184.0	1226.0
^{147}Sm	0.5	108.5	41.2	48.2	61.8	46.8	155.8	130.4	207.0	37.0	202.8
^{153}Eu	0.5	17.2	8.4	9.8	11.2	5.7	16.0	7.7	10.3	0.7	14.8
^{157}Gd	0.5	78.2	29.8	34.8	54.4	42.7	129.3	105.7	172.2	34.3	171.2
^{159}Tb	0.5	9.9	3.2	3.6	5.9	5.0	15.1	11.8	20.7	4.5	21.9
^{163}Dy	0.5	54.9	18.2	20.1	35.3	25.9	82.2	63.9	121.4	26.6	135.9
^{166}Er	0.5	27.6	11.5	11.6	21.8	14.2	38.4	31.5	58.5	14.6	83.4
^{169}Tm	0.5	3.5	1.8	1.6	3.2	2.0	4.9	3.3	6.9	2.0	12.8
^{172}Yb	0.5	23.0	16.4	10.5	22.9	13.2	29.3	20.6	39.6	11.4	90.6
^{175}Lu	0.5	3.4	3.2	2.2	4.1	2.4	4.4	3.0	5.8	1.5	16.2
^{177}Hf	0.5	<DL	2.4	<DL	<DL	<DL	<DL	<DL	<DL	<DL	<DL
^{204}Pb	0.5	11.0	8.8	1.4	6.4	<DL	9.0	16.0	7.0	0.9	4.7
^{206}Pb	0.5	12.4	4.1	3.9	3.9	2.6	1.9	5.3	0.9	<DL	2.3
^{207}Pb	0.5	2.2	1.2	1.0	1.1	1.0	1.0	1.4	0.6	<DL	1.1
^{208}Pb	0.5	4.7	2.1	1.5	2.0	1.4	1.2	1.4	0.6	<DL	1.4
^{232}Th	0.5	187.8	61.3	40.7	52.5	10.7	1.9	13.6	4.7	1.1	15.7
^{235}U	0.5	349.0	80.0	81.0	82.0	41.0	21.4	119.0	9.3	1.5	27.4
^{238}U	0.5	98.2	22.8	24.1	23.0	11.4	5.4	35.2	3.2	0.6	8.9

Apatite formulas were calculated on the basis of five atoms of Al, Ce, Fe, Mn, Mg, Ca, Na. We assumed that Si and S substitute for P (Elliot, 1994). DL = detection limit.

Table 2: Cont.

Batholith	Takomkane										
Unit	Spout Lake	Buster Lake	Boss Creek	Woodjam Creek	Schollhouse Lake	Schollhouse Lake	Schollhouse Lake	Schollhouse Lake	Schollhouse Lake	Schollhouse Lake	Qtz-feldspar porphyry
Rock	monzodiorite	gabbro	monzodiorite	qtz monzonite	granodiorite	granodiorite	granodiorite	granodiorite	granodiorite	granodiorite	QFP
CL Color	olive green	dark green	olive green	dark brown	brown	brown	dark brown	greenish brown	brown	green	brown
Sample#	15FB-28	15FB-33	15FB-29	10FB-01	15Fb-37	15FB-36	15FB-36	15FB-36	15FB-36	15FB-36	15FB-35
Analysis#	P03-03-4	P03-02a-2	P03-01-2	P11-06a-2	P03-07-10-1	P03-08b-9-1	P03-09-6-1	P03-09-6-2	P03-09-6-3	P03-09-6-4	P03-04a-5
Electorn-probe microanalysis (wt.%):											
Na_2O	0.05	0.03	0.10	0.19	0.05	0.13	0.14	0.10	0.08	0.07	0.04
MgO	0.03	0.02	0.03	0.02	<DL	0.00	0.03	0.00	0.03	0.09	0.01
Al_2O_3	0.00	<DL	0.01	0.02	<DL	0.01	0.01	0.01	<DL	0.09	<DL
SiO_2	0.18	0.06	0.17	0.21	0.13	0.21	0.17	0.02	0.18	0.32	0.13
P_2O_5	42.13	42.28	42.29	41.25	42.92	42.96	42.55	42.23	42.16	42.33	41.44
SO_3	0.17	0.04	0.22	0.39	0.21	0.37	0.48	0.32	0.13	0.16	0.07
CaO	55.10	55.16	55.50	55.52	56.08	55.98	55.30	56.26	55.13	55.31	55.41
MnO	0.11	0.10	0.25	0.15	0.10	0.20	0.13	0.06	0.14	0.09	0.15
FeO	<DL	<DL	<DL	0.14	0.02	0.00	<DL	0.01	0.03	0.07	0.06
Ce_2O_3	0.11	<DL	0.14	0.29	0.14	0.27	<DL	0.06	0.30	<DL	<DL
Cl	0.36	0.76	0.23	0.78	0.04	0.01	0.14	0.09	0.10	0.05	0.38
Total	98.24	98.44	98.93	98.96	99.68	100.14	98.94	99.16	98.30	98.58	97.71
Atomic formulae calculation (per formula unit):											
Na^{+}	0.008	0.005	0.016	0.031	0.008	0.021	0.022	0.016	0.013	0.011	0.007
Mg^{2+}	0.004	0.002	0.004	0.003	<DL	0.000	0.003	0.001	0.004	0.011	0.002
Al^{3+}	0.000	<DL	0.001	0.002	<DL	0.001	0.001	0.001	<DL	0.009	<DL
Ca^{2+}	4.976	4.986	4.958	4.935	4.980	4.956	4.964	4.976	4.962	4.957	4.976
Mn^{2+}	0.008	0.007	0.018	0.011	0.007	0.014	0.009	0.004	0.010	0.007	0.011
Fe^{2+}	<DL	<DL	<DL	0.010	0.001	0.000	<DL	0.001	0.002	0.005	0.004
Ce^{3+}	0.003	<DL	0.004	0.009	0.004	0.008	<DL	0.002	0.009	<DL	<DL
Subtotal	5.000	5.000	5.000	5.000	5.000	5.000	5.000	5.000	5.000	5.000	5.000
P^{5+}	3.006	3.021	2.985	2.897	3.012	3.005	3.019	2.951	2.998	2.998	2.941
Si^{4+}	0.015	0.005	0.015	0.018	0.011	0.017	0.015	0.002	0.015	0.027	0.011
S^{6+}	0.027	0.007	0.035	0.061	0.032	0.057	0.075	0.050	0.021	0.025	0.012
Subtotal	3.048	3.032	3.034	2.976	3.055	3.080	3.108	3.003	3.035	3.050	2.964
Cl^{-}	0.051	0.109	0.032	0.109	0.006	0.002	0.019	0.013	0.015	0.007	0.054
LA-ICP-MS microanalysis (ppm):											
^{23}Na	153.0	44.3	429.0	978.0	257.0	352.0	507.0	329.0	266.0	<DL	126.0
^{27}Al	14.0	2.1	<DL	0.6	1.7	<DL	140.0	51.0	<DL	<DL	<DL
^{29}Si	1060.0	300.0	240.0	<DL	770.0	400.0	1140.0	1710.0	1180.0	<DL	1060.0
^{30}Si	5600.0	7900.0	8400.0	2200.0	1700.0	3300.0	6600.0	18200.0	<DL	<DL	<DL
^{51}V	3.0	1.3	1.1	30.7	0.8	0.7	<DL	0.9	0.7	<DL	1.7
^{55}Mn	57.7	33.1	121.5	1435.0	54.8	111.2	74.9	82.3	82.6	<DL	58.6
^{63}Cu	8.9	13.1	<DL	<DL	<DL	<DL	<DL	<DL	<DL	<DL	<DL
^{88}Sr	43.7	121.6	46.0	335.3	36.2	58.3	49.0	80.4	71.7	<DL	46.8
^{89}Y	21.2	9.1	21.8	561.7	11.2	15.7	10.2	20.7	19.3	<DL	20.2
^{90}Zr	<DL	<DL	<DL	1.2	8.5	<DL	<DL	<DL	<DL	<DL	<DL
^{91}Zr	<DL	<DL	<DL	0.9	7.4	<DL	<DL	<DL	<DL	<DL	<DL
^{139}La	25.8	8.5	38.4	791.0	27.8	38.0	23.0	41.9	42.7	<DL	36.1
^{140}Ce	59.3	20.2	83.9	1675.0	39.7	62.8	41.1	82.7	78.7	<DL	71.0
^{141}Pr	7.3	2.9	10.3	212.4	3.6	6.2	4.5	9.3	8.1	<DL	7.9
^{146}Nd	31.4	14.1	42.2	953.0	13.8	23.2	17.7	37.3	29.3	<DL	30.9
^{147}Sm	6.1	3.3	7.2	178.8	2.4	4.0	3.0	6.2	4.8	<DL	5.6
^{153}Eu	0.8	0.7	1.0	18.7	<DL	0.7	<DL	1.1	0.8	<DL	1.0
^{157}Gd	5.9	3.2	6.4	151.8	2.5	3.6	2.5	5.5	4.2	<DL	4.8
^{159}Tb	0.7	<DL	0.8	20.0	<DL	<DL	<DL	0.7	0.5	<DL	0.6
^{163}Dy	4.0	2.0	4.2	111.3	1.8	2.6	1.8	3.6	3.0	<DL	3.3
^{166}Er	2.2	0.8	2.2	55.5	1.2	1.6	1.0	2.1	1.9	<DL	2.1
^{169}Tm	<DL	<DL	<DL	7.1	<DL	<DL	<DL	<DL	<DL	<DL	<DL
^{172}Yb	2.2	0.5	1.8	39.2	1.1	1.6	0.8	1.8	1.8	<DL	2.2
^{175}Lu	<DL	<DL	<DL	5.5	<DL	<DL	<DL	<DL	<DL	<DL	<DL
^{177}Hf	<DL	<DL	<DL	<DL	<DL	<DL	<DL	<DL	<DL	<DL	<DL
^{204}Pb	<DL	<DL	1.5	6.0	1.3	0.5	<DL	1.0	<DL	<DL	<DL
^{206}Pb	<DL	<DL	<DL	1.7	<DL	<DL	<DL	<DL	<DL	<DL	<DL
^{207}Pb	<DL	<DL	<DL	1.3	<DL	<DL	<DL	<DL	<DL	<DL	<DL
^{208}Pb	<DL	<DL	<DL	1.3	<DL	<DL	<DL	<DL	<DL	<DL	<DL
^{232}Th	2.7	1.9	0.7	13.0	0.6	0.6	<DL	0.9	1.1	<DL	2.2
^{235}U	6.3	3.0	1.0	10.6	1.4	0.7	<DL	0.9	2.1	<DL	3.7
^{238}U	1.8	1.2	<DL	5.2	0.5	<DL	<DL	<DL	0.5	<DL	1.4

Table 3: Representative analyses of titanite from the Guichon Creek and Takomkane batholiths.

Batholith	Detection limit	Guichon Creek							
Unit		Border	Border-Guichon	Guichon	Chataway	Bethlehem	Skeena	Bethsaida	Aplite
Rock		granodiorite	granodiorite	granodiorite	granodiorite	granodiorite	granodiorite	granodiorite	aplite
Color		pale yellow	dark brown	honey	dark brown	honey brown	honey brown	honey yellow	pale brown
Sample#		2238923	2238840	15FB-07	2238899	15FB-19	2238818	2238791	15FB-13
Analysis#		P08-10-9-1	P18-04-10	P23-02-14-1	P14-07-3-1	P14-03-6-1	P06-06-6-2	P14-04-5-2	P18-05b-4-1
Electorn-probe microanalysis (wt.%):									
Na_2O	0.04 (%)	<DL	<DL	<DL	<DL	<DL	0.04	<DL	<DL
MgO	0.03	<DL	<DL	<DL	0.03	<DL	<DL	<DL	<DL
Al_2O_3	0.02	1.10	1.13	0.80	0.89	0.83	0.80	0.95	1.00
SiO_2	0.02	29.73	29.86	29.82	29.38	29.53	29.01	29.83	30.04
CaO	0.24	27.31	27.92	28.27	26.48	26.95	26.30	26.99	28.31
TiO_2	0.14	38.35	36.68	38.06	36.69	37.34	38.18	35.96	36.53
V_2O_5	0.08	0.20	0.18	0.18	0.21	0.20	0.12	0.20	0.13
MnO	0.07	<DL	0.11	0.12	0.11	0.14	0.24	0.32	0.20
FeO	0.08	1.19	1.73	1.12	1.36	1.23	1.57	2.27	1.85
Total		97.89	97.61	98.36	95.12	96.22	96.25	96.53	98.05
Atomic formulae calculation (per formula unit) based on O = 5									
Na^{+}		<DL	<DL	<DL	<DL	<DL	0.001	<DL	<DL
Mg^{2+}		<DL	<DL	<DL	0.001	<DL	<DL	<DL	<DL
Al^{3+}		0.043	0.045	0.031	0.036	0.033	0.032	0.038	0.039
Si^{4+}		0.991	1.001	0.992	1.007	1.001	0.985	1.011	1.004
Ca^{2+}		0.975	1.003	1.008	0.972	0.979	0.957	0.980	1.014
Ti^{+4}		0.961	0.925	0.952	0.946	0.952	0.975	0.916	0.918
V^{5+}		0.005	0.004	0.004	0.005	0.005	0.003	0.004	0.003
Mn^{2+}		<DL	0.003	0.003	0.003	0.004	0.007	0.009	0.006
Fe^{2+}		0.030	0.044	0.028	0.035	0.031	0.040	0.058	0.046
LA-ICP-MS microanalysis (ppm):									
^{23}Na	0.5 (ppm)	108	35	83.7	82.1	86.3	124.9	92.7	56
^{25}Mg	0.5	910	200	242	95	116	85	68.3	56.1
^{27}Al	0.5	16400	4644	3648	3623	3564	3429	3756	3608
^{51}V	0.5	2872	874	803	716.3	662.2	666	534.3	739.4
^{55}Mn	0.5	763	704.3	743.3	611.7	<DL	1159	1569	796
^{57}Fe	0.5	8920	7520	4519	6320	5740	5680	7080	7120
^{63}Cu	0.5	11.1	2.99	30.9	0.66	0.59	0.54	0.82	1.57
^{88}Sr	0.5	67	22.4	21.88	27.9	31.5	22.1	6.15	11.87
^{89}Y	0.5	2900	571.1	253.8	2066	1227	2372	1943	213.9
^{90}Zr	0.5	741	220.2	301	436.6	868	492.3	534.4	215.6
^{91}Zr	0.5	663	342	305	431	685	507	545	189.4
^{139}La	0.5	1780	926	1155	1884	1596	2437	1836	487
^{140}Ce	0.5	5600	2531	1950	7621	6634	7710	5717	1011
^{141}Pr	0.5	814	304.7	125.7	1108.1	565.2	933	676.4	110.1
^{146}Nd	0.5	3710	1081	414.7	5213	3554	3933	2279	422.9
^{147}Sm	0.5	1090	175.4	72.5	910	499	565.8	313.2	62.3
^{153}Eu	0.5	163	59.8	18.02	130.7	62.9	104.8	33.13	19.64
^{157}Gd	0.5	386	114.6	61.2	524	244.3	517	254	40.1
^{159}Tb	0.5	96.1	15.86	7.64	71.5	31.5	67.8	35.54	5.46
^{163}Dy	0.5	625	102.7	46.8	419.4	193.7	398.1	264.1	34.8
^{166}Er	0.5	434	62.6	27.1	224.5	<DL	225.3	198.5	21.9
^{169}Tm	0.5	53.9	10.52	4.26	32.44	19.95	36.65	33.39	3.6
^{172}Yb	0.5	368	80.1	39.6	216	152.4	255.9	236.7	25.2
^{175}Lu	0.5	63.2	12.72	8.05	28.09	21.81	34.46	33.62	4.71
^{177}Hf	0.5	67.2	25.1	32.6	42.8	94	63.6	105.5	6.29
^{204}Pb	0.5	<DL	2.5	<DL	8.4	10	2	<DL	2
^{206}Pb	0.5	212	55.6	15.78	10.18	13.13	6.73	2.82	13.44
^{207}Pb	0.5	20.2	3.96	1.7	1.06	0.88	1.16	0.62	1.12
^{208}Pb	0.5	34.4	4.45	9.96	9.7	7.98	5.83	1.795	4.01
^{232}Th	0.5	1110	177.4	503	489.5	382.6	287.5	62.98	190.8
^{235}U	0.5	4130	1168	298	260	243	190	42.1	318
^{238}U	0.5	1640	403.2	111.9	73	64.69	45.78	14.96	93.6

Table 3: Cont.

Batholith	Takomkane					
Unit	Spout Lake	Buster Lake	Boss Creek	Woodjam Creek	Schollhouse Lake	Qtz-feldspar porphyry
Rock	monzodiorite	gabbro	monzodiorite	qtz monzonite	granodiorite	qtz-feldsapr porphyry
Color	brown	greenish-yellow	greenish-yellow	dark brown	brown	greenish-yellow
Sample#	15FB-26	15FB-33	15FB-29	10FB-01	15Fb-37	15FB-35
Analysis#	P22-07b-4-1	P04-05a-5-1	P04-02-13-2	P07-08-12-1	P07-03a-10-1	P04-07-6-1
Electorn-probe microanalysis (wt.%):						
Na_2O	<DL	<DL	<DL	<DL	<DL	<DL
MgO	<DL	<DL	<DL	<DL	<DL	<DL
Al_2O_3	0.90	0.72	0.84	0.75	1.35	1.10
SiO_2	29.63	29.43	29.18	29.12	30.27	29.82
CaO	27.06	27.44	27.58	27.22	28.42	27.49
TiO_2	36.59	37.73	36.53	36.44	37.56	36.11
V_2O_5	0.13	0.21	0.13	0.13	0.19	0.18
MnO	0.17	<DL	0.19	0.17	0.14	0.15
FeO	1.49	0.86	1.10	1.67	1.50	1.47
Total	95.96	96.40	95.56	95.50	99.44	96.33
Atomic formulae calculation (per formula unit) based on O = 5						
Na^{+}	<DL	<DL	<DL	<DL	<DL	<DL
Mq^{2+}	<DL	<DL	<DL	<DL	<DL	<DL
Al^{3+}	0.036	0.029	0.034	0.030	0.053	0.044
Si^{4+}	1.008	0.997	0.999	0.998	0.996	1.011
Ca^{2+}	0.987	0.995	1.012	1.000	1.002	0.999
Ti^{+4}	0.936	0.961	0.941	0.940	0.929	0.921
V^{5+}	0.003	0.005	0.003	0.003	0.004	0.004
Mn^{2+}	0.005	<DL	0.005	0.005	0.004	0.004
Fe^{2+}	0.038	0.022	0.028	0.043	0.037	0.038
LA-ICP-MS microanalysis (ppm):						
^{23}Na	137	19.7	29.9	102.8	28.9	214
^{25}Mg	113	47.8	83	147	50.3	12.3
^{27}Al	3486	2418	2410	4284	4759	5580
^{51}V	476	520.6	358.8	1071	760	1416
^{55}Mn	1072	316.8	1050	1873	878	2490
^{57}Fe	5970	1873	3383	5820	5460	326
^{63}Cu	30	0.54	4.18	2.5	0.51	6.9
^{88}Sr	39	21.7	46.4	9.3	11.32	172
^{89}Y	1363	1380	682.3	1116	225	15100
^{90}Zr	1076	204.4	421.9	1994	104.8	1150
^{91}Zr	1163	230	561	1591	112.2	255
^{139}La	1295	519	727.4	1364	528	9160
^{140}Ce	2332	1534	1902	2342	892	26300
^{141}Pr	266.7	245	184.9	225	68.5	5220
^{146}Nd	987	1274	940.6	1009	270	4260
^{147}Sm	217.3	276.4	139.2	324	39.2	793
^{153}Eu	63.5	76.3	34.11	38.1	22.44	587
^{157}Gd	213.5	219	139.3	225.6	42.9	725
^{159}Tb	33.11	38.65	16.74	48.5	4.2	752
^{163}Dy	207.3	260.1	114.6	251.5	36.5	1066
^{166}Er	149.1	140.7	81.9	150.9	23.6	784
^{169}Tm	24.07	21.74	13.32	24.49	4.16	342
^{172}Yb	178.5	153.1	90.3	230.2	41.3	454
^{175}Lu	28.22	17.28	17.21	25.52	6.88	265
^{177}Hf	85	15	33.7	116	13.7	72.2
^{204}Pb	18	2	<DL	<DL	8.9	0.54
^{206}Pb	149	8.22	8.89	222.3	12.4	39.1
^{207}Pb	35	0.538	1.11	14.35	1.07	6.9
^{208}Pb	44	3.05	3.87	29.8	0.99	51.3
^{232}Th	485	155.7	230.2	1184	33.4	3650
^{235}U	2620	262	271	16000	331	7.6
^{238}U	767	66.4	55.02	2109	97	1101

Triassic-Early Jurassic units of the Takomkane batholith have gabbro (Buster Lake) and diorite (Boss Creek) compositions whereas the Early Jurassic Woodjam and Schoolhouse Lake units have granodiorite compositions. One sample of the younger Quesnel unit has gabbroic composition.

At Granite Mountain, the Burgess Creek stock unit, including the units mapped as Burgess mixed unit, has diverse composition of gabbro and granodiorite-granite suggesting that this stock represents a mixed body of mafic and felsic phases. The Mine phase and the Granite Mountain phases have similar composition of diorite to granite but largely granodiorite similar to the Early Cretaceous Sheridan Creek stock.

Total alkali-silica (TAS) diagram (Fig. 9) indicates that samples from the Guichon Creek, Takomkane and Granite Mountain batholiths follow a calc-alkaline trend from gabbro to granodiorite and granite. Major element compositions of the various rock units of the three batholiths range from 45 to 78 wt. % SiO_2 (Fig. 10). The mafic units that typically occur as the border phases have ca. 45 to 60% SiO_2 whereas more felsic units are between ~ 60 to 78% SiO_2. K_2O and Na_2O concentrations have scattered distributions, possibly due to weak alteration, but otherwise are more sodic than potassic. In both mafic and felsic units, the concentration of CaO, FeO (total), MgO, Al_2O_3 and TiO_2 decreases with increase of silica in all three batholiths. Similar relationships can be seen for P_2O_5 in Guichon Creek and Takomkane batholiths but not in the Granite Mountain batholith. This general trend is attributed to the intrusive rocks becoming progressively evolved, i.e., more silica rich with increasing fractionation, in each batholith as they become younger.

There are notable increases in Al_2O_3 concentrations relative to TiO_2 in the Bethlehem and Bethsaida phases of the Guichon Creek batholith (Fig. 11) as previously noted by D'Angelo et al. (2017). A similar relationship is apparent at Granite Mountain where some of the Granite Mountain and Mine Phases trend to become more Al-rich. Such a trend is not obvious at Takomkane perhaps because of the limited available data. There is, however, an inverse relationship between Ti and Al within the Woodjam samples (Fig. 11). The increase of Al/Ti is attributed to the onset of suppression of plagioclase fractionation and the crystallization of amphibole in wet (hydrous) fertile magmas (Loucks, 2014).

REE Characteristics

Trace-element and rare-earth element data (Table 1) were normalized to the compositions of C1 carbonaceous chondrite meteorites using the values of Sun and McDonough (1989). Normalized rare-earth element (REE) diagrams show that all samples are characterized by relatively high REE content, up to 100x chondrite, and are generally enriched in light REE (LREE) relative to heavy rare-earth elements (HREE); Fig. 12). At Guichon Creek, the Border, Guichon and Chataway phases have greater REE relative to the later Bethlehem, Skeena and Bethsaida phases. But the late aplite dike has the most enriched REE concentrations. Similar relationship cannot be established for various plutonic phases at Takomkane and Granite Mountain batholiths.

Plagioclase crystallization preferentially incorporates Eu^{2+} over Eu^{3+} and typically results in more fractionated rocks having negative Eu anomalies (Burnham et al., 2015). All rock units at Guichon Creek batholith lack a significant Eu anomaly ($Eu_n/Eu^* > 0.75$) or show a weak positive Eu anomaly, except for the late aplite dike which has a pronounced negative Eu anomaly (Fig. 12). The Eu anomaly does not correlate with the SiO_2 content of the rock. Similar relationships can be seen for the rock units of the Takomkane batholith. At Granite Mountain, the Burgess unit and the Border phase have variable Eu anomaly from positive to negative. The Granite Mountain and the Mine phase ranges from minimal to a strongly negative Eu anomaly which correlates with increasing SiO_2. The minimal Eu anomaly for Guichon Creek and Takomkane batholith units suggest an influence from high magmatic water content and high oxidation state (Lang and Titley, 1998; Richards, 2012; Loucks, 2014) with minimal effect by fractional crystallization except for the late aplite dikes. Granite Mountain rocks have variably negative Eu anomalies suggesting variable degrees of plagioclase fractionation.

Most samples from the three batholiths show moderate LREE enrichments (La/Sm_n = 2 to 4) with stronger LREE enrichments in Guichon Creek (2 to 6, Fig. 12). One sample of the Buster Lake unit of the Takomkane and two samples of Burgess Creek and Border phase at Granite Mountain, however, have nearly flat REE patterns that are typical of more primitive magmas. Samples of the Guichon Creek batholith have weak MREE enrichments relative to HREE (Dy/Yb_n = 1 to 1.5) and Takomkane and Granite Mountain samples show no significant enrichments or depletions. These relationships suggest that hornblende and/or garnet crystallization controlled the REE distribution (Bissig et al., 2017).

A plot of Sr/Y relative to Y show distinct variations (Fig. 12). At Guichon Creek there is a trend from higher Sr/Y to lower Y contents, as also shown by D'Angelo et al., (2017). Mineralized host rocks of the Bethsaida, Bethlehem and Skeena have higher Sr/Y (>50) but lower Y contents relative to other rock units (<10 ppm). The youngest phases of the batholith, aplite dikes and Spatsum granodiorite, have the lowest Sr/Y and highest Y concentrations. Similar trends occur in the Takomkane and Granite Mountain batholiths but there is considerable overlap of the main mineralized phases with other units. The variations of Sr/Y ratio is attributed to high water pressure during crystallization of magma which suppresses plagioclase crystallization, resulting in higher Sr in the melt while facilitating hornblende crystallization, thus causing lower Y (Rohrlach and Loucks, 2005).

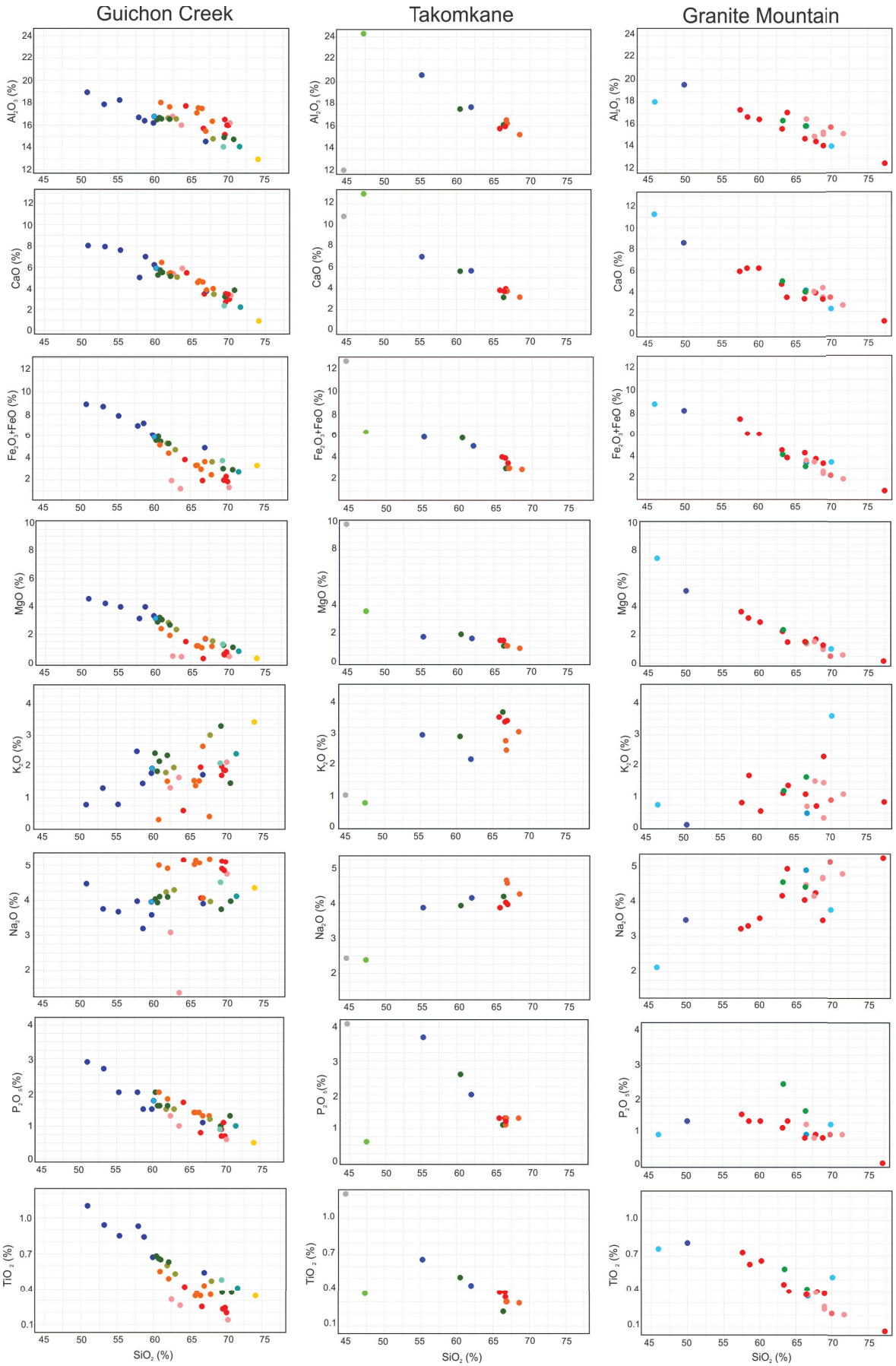

Figure 10: Harker diagrams for samples from Guichon Creek, Takomkane and Granite Mountain batholiths. Coloured symbols represent rock units as shown in Figure 9.

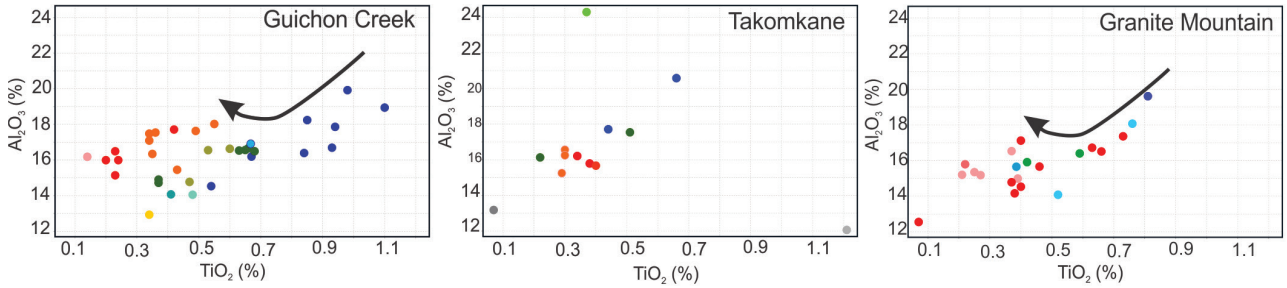

Figure 11: Plot of Al_2O_3 vs. TiO_2 for the Guichon Creek, Takomkane and Granite Mountain batholiths showing the increase of Al_2O_3 in more fertile plutons. Coloured symbols represent rock units as shown in Figure 9.

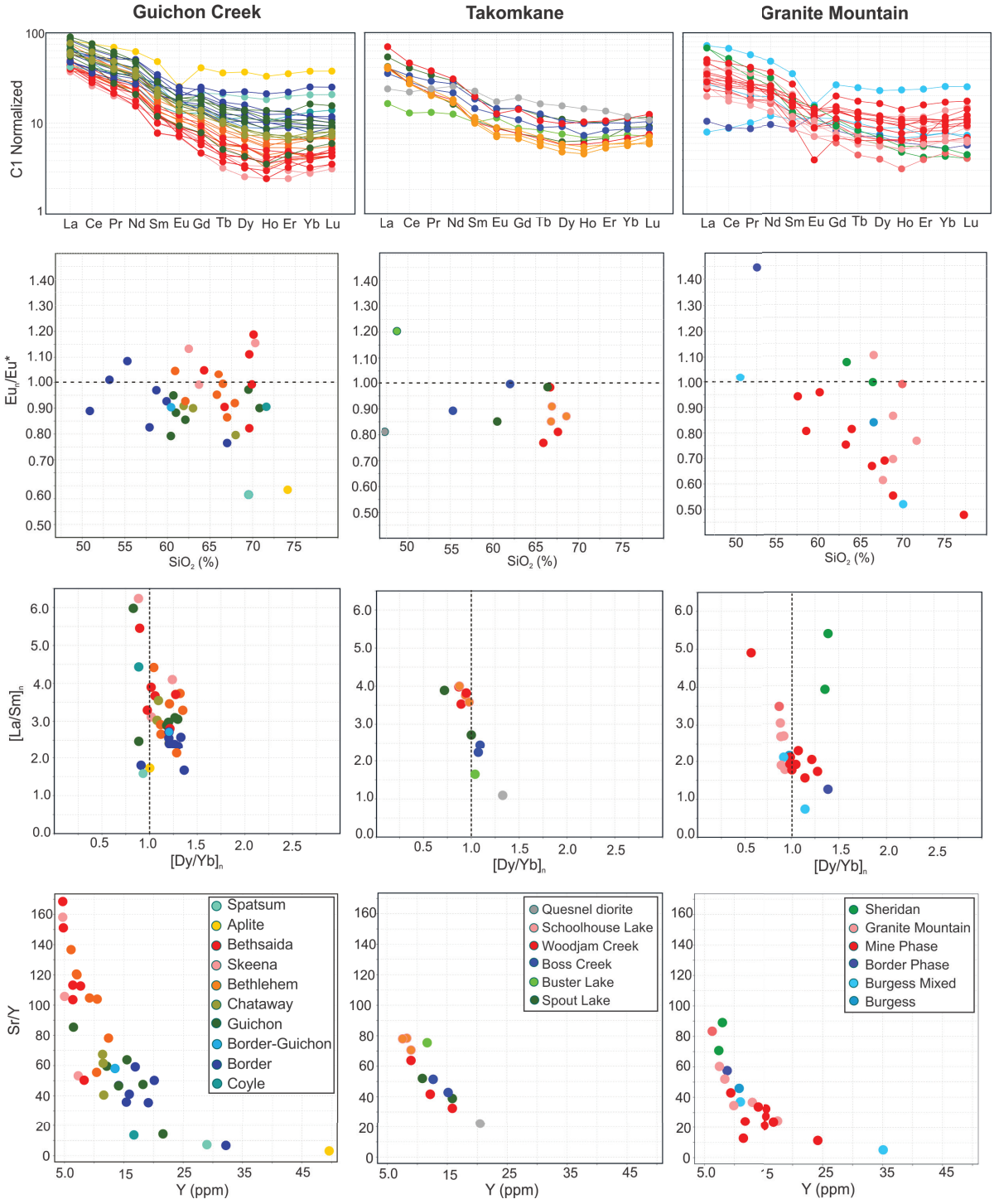

Figure 12: REE and trace element characteristics of Guichon Creek, Takomkane and Granite Mountain batholiths.

APATITE AND TITANITE TEXTURE

Apatite textures were studied using cathodoluminescence (CL) microscopy, and titanite by scanning electron microscopy (SEM). Apatite grains are colourless and commonly have hexagonal crystal shapes; most grains were around 100 micron in length. Apatites in the studied samples have brown, green or yellow luminescence. Concentric zoning is common and forms alternating zones of dark-brown, brown, greenish-brown and green luminescence. In many samples, it occurs with light brown cores surrounded by darker brown zones (Fig. 13a). Some grains have dark-brown cores (Fig. 14). Green luminescent rims are common (Fig. 13b). The apatite grains in largely non-mineralized phases have uniform to zoned brown luminescence (Fig. 13a). The green-luminescent apatite typically has dark brown cores that are zoned outward to green-brown– and green-luminescent apatite (Fig. 14). Apatite grains in mineralized units, particularly the Bethsaida phase of the Guichon Creek batholith, the Woodjam Creek unit of the Takomkane batholith and the Mine phase of the Granite Mountain batholith, have well-developed green luminescence (Fig. 13c). Locally, the entire apatite grain has green luminescence. Spot analysis of apatite zones shows that the brown luminescent cores have higher Cl and S relative to the green luminescent rim (Fig. 13).

Titanite is a common accessory mineral comprising about 2–4% in various phases of the studied batholiths. Titanite grains are 1–2 mm, range from colourless to dark brown and locally contain inclusions of an opaque phase, most typically ilmenite. Less commonly, inclusions of apatite, zircon and quartz are also noted (Fig. 13d). Titanite textures under SEM vary from uniform to zoned, and more rarely display irregular mottled rims. The zoning is difficult to see even under SEM. Spot analysis indicate that rims have higher Fe:Al and Mn:Ca relative to core (Fig. 13). Titanite grains in the Granite Mountain batholith were typically smaller and fewer than those in other batholiths and it was not possible to collect representative grains from some phases of the batholith; therefore Granite Mountain titanites are not further discussed.

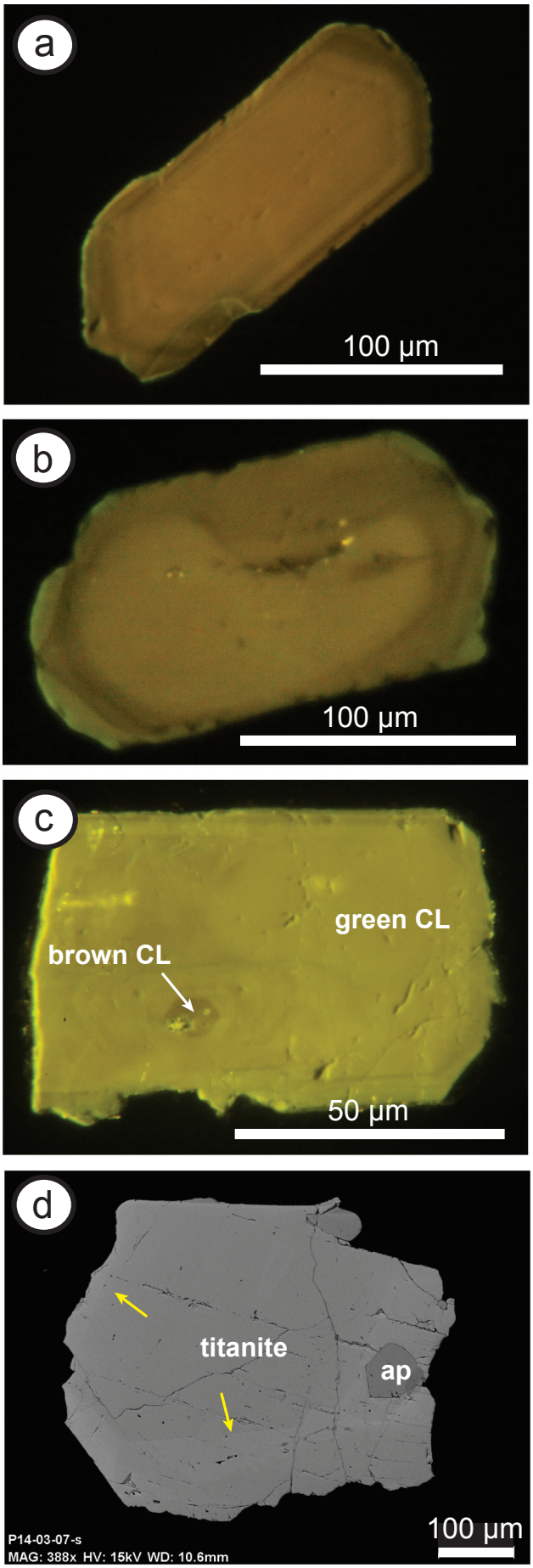

Figure 13: Cathodoluminescence images of apatite grains and SEM image of titanite: (a) zoned apatite with light brown to brown luminescence from the Spout Lake pluton, Takomkane batholith; (b) apatite from the Granite Mountain phase of the Granite Mountain batholith with brown luminescence and narrow green luminescence developed at the rim; (c) apatite from the Bethsaida phase of the Guichon Creek batholith, showing a small brown luminescent core surrounded by yellow-green luminescent apatite; and (d) back scattered electron (BSE) image of a zoned titanite grain from the Bethlehem phase of the Guichon Creek batholith. The rim shown by arrows has higher Fe/Al and Mn/Ca ratios relative to the core.

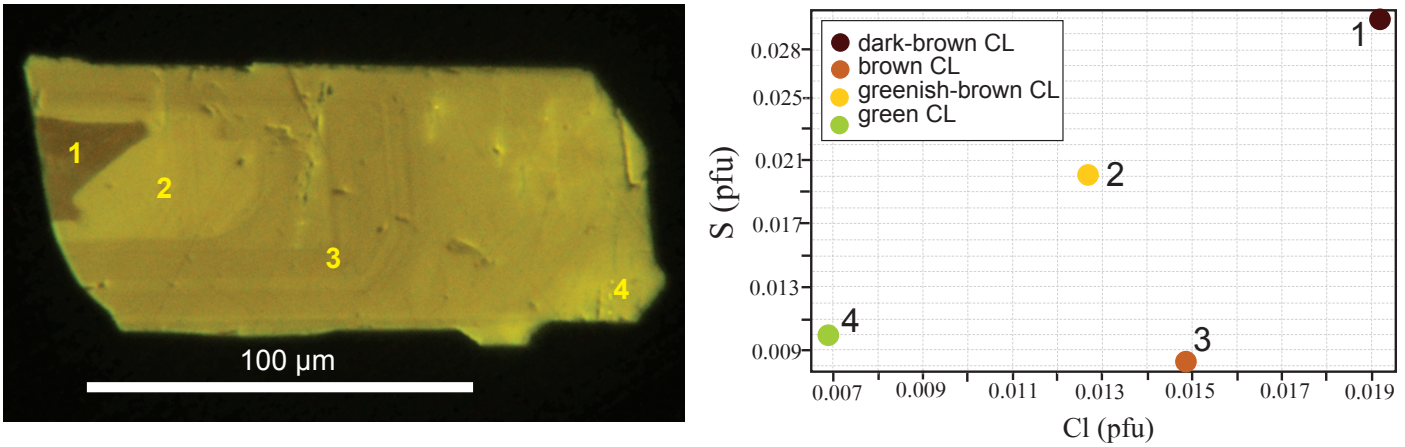

Figure 14: Correlation of apatite texture with composition: (left) zoned apatite from the Woodjam Creek unit of the Takomkane batholith, showing a core with brown luminescence and a rim with green luminescence; numbers represent location of spots analyzed by EPMA; (right) binary diagram showing correlation of apatite luminescence in grain shown in Figure 14a.

APATITE COMPOSITION

Chlorine and Sulphur in Apatite

Apatites from the mineralized plutons have distinct trace element characteristics compared to non-mineralized plutons (Table 2). At Guichon Creek batholith, the Border, Guichon and Chataway phases have apatite with Cl concentration > 0.05 pfu (0.35 wt%) whereas the apatite from the Bethlehem, Skeena and Bethsaida have < 0.05 pfu Cl and mostly below detection limit (0.003 pfu: Fig. 15a). The S concentration varies from below detection limit (0.011 pfu or 0.17% wt% oxide) to 0.092 pfu (0.58%). Apatite in all phases have a range of S concentrations from low to high except for the mineralized Bethsaida phase which has distinctly lower S concentrations (<0.045 pfu or 0.28%: Fig. 15a). Apatite rims typically have lower S and Cl concentrations, particularly in mineralized plutonic phases. Thus, apatite rims from the Bethlehem and Skeena phases have low S concentrations similar to those apatite rims from the Bethsaida phase (Fig. 15c).

At the Takomkane batholith, apatites from the main mineralized Woodjam Creek phase have a range of Cl and S concentration from high to low with a positive correlation between Cl and S (Fig. 16a). The Cl concentration varies from 0.15 pfu (1.0%) to below detection limit and S concentration varies from 0.11 pfu (0.73%) to below detection limit. The Spout Lake pluton apatites have a similar range but with slightly lower S and Cl concentrations. Apatites from the Boss Creek and Schoolhouse Lake units have similar S variations to those in Woodjam Creek but with distinctly lower Cl concentration (below ca. 0.03 pfu or 0.2%). Zoned apatite occurs in all plutons, with apatite rims having notably less Cl and S compared to apatite cores (Fig. 16c).

At the Granite Mountain batholith, apatites have a scatter of S and Cl concentrations (Fig. 17a). However, apatites from the Burgess Creek and Burgess Creek Mixed units have higher S and Cl concentrations with Cl up to 0.098 pfu (0.7%) and S up to 0.089 pfu (0.56%), whereas apatites from the Granite Mountain and the Mine phase have lower S and Cl concentrations with Cl below 0.035 pfu (0.25%) and S below 0.05 pfu (0.3%). Moreover, the apatite rims have even lower S and Cl concentrations (Fig. 17c).

Apatite Luminescence Indicators

Apatite grain compositions were compared with their luminescence. Apatites studied display luminescence colours including dark brown, brown, greenish-brown, dark green, green, greenish yellow and yellow (see Fig. 14). Apatites with green luminescence, either dark green or green, are those with depleted S and Cl, whereas those apatites with brown luminescence (either dark brown, brown or greenish brown) have variable S and Cl concentrations. The exact cause of this change in luminescence colour is not known. In single apatite grains, the brown luminescent apatite has higher S and Cl concentration than green luminescent apatite (Fig. 14) but all brown luminescent apatites do not have similar S or Cl concentrations. Despite these complexities, these correlations between apatite composition and luminescence colour occurs in all three batholiths (Fig. 15b, 16b, and 17b). This is particularly well characterized by the compositional zoning in the data from dark brown-brown luminescent apatite with the highest S and Cl, to the greenish brown-greenish yellow luminescent apatite with intermediate S and Cl concentration, and then to dark green-green luminescent apatite with the lowest S and Cl concentrations.

Other trace elements in apatite such as V and Na are not discussed here, but also show similar relationships with Cl. Figure 18 illustrates that mineralized plutons have distinctly lower V in their apatite.

REE in Apatite

The REE concentration in apatite (Table 2) is characterized by high LREE and MREE concentrations relative to HREE and

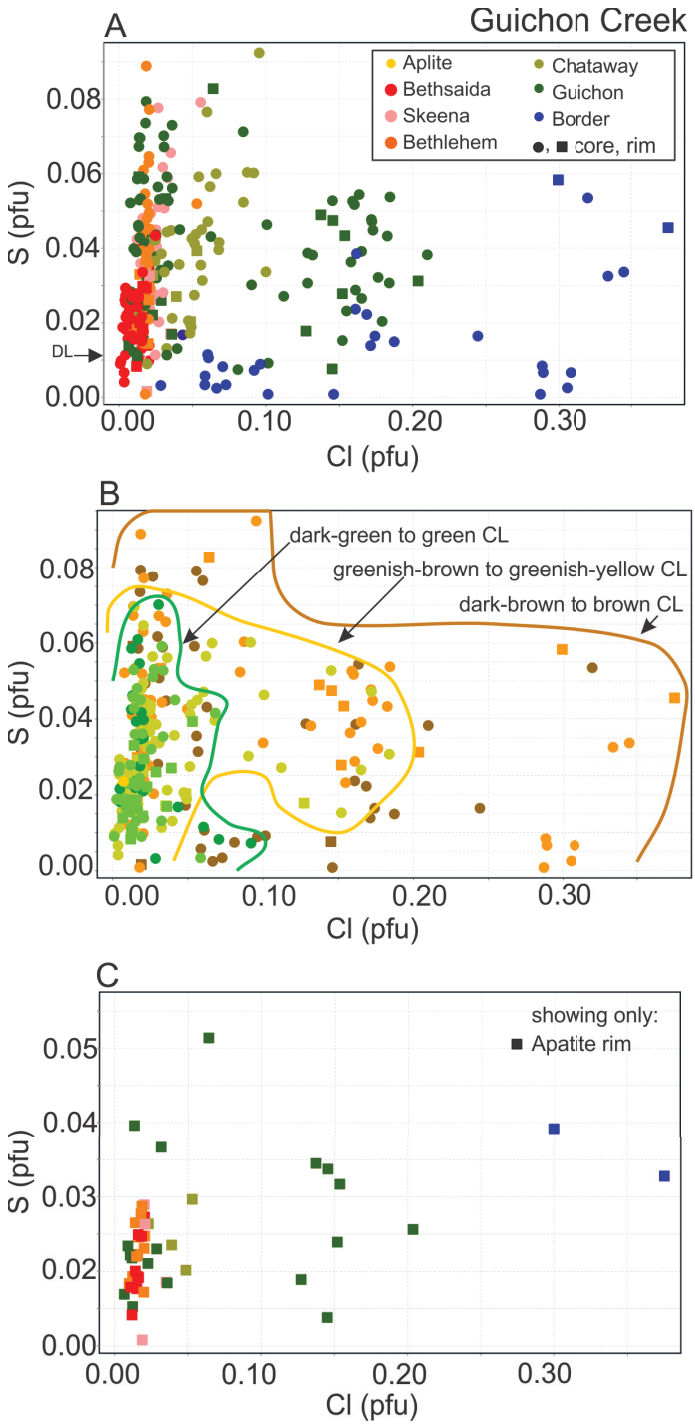

Figure 15: a) Chlorine and sulphur variation in apatite from Guichon Creek batholith. (b) Same diagram as in Fig. 15a but showing the luminescence color of grains. (c) Same as in Fig. 15a but showing only results from the apatite rim.

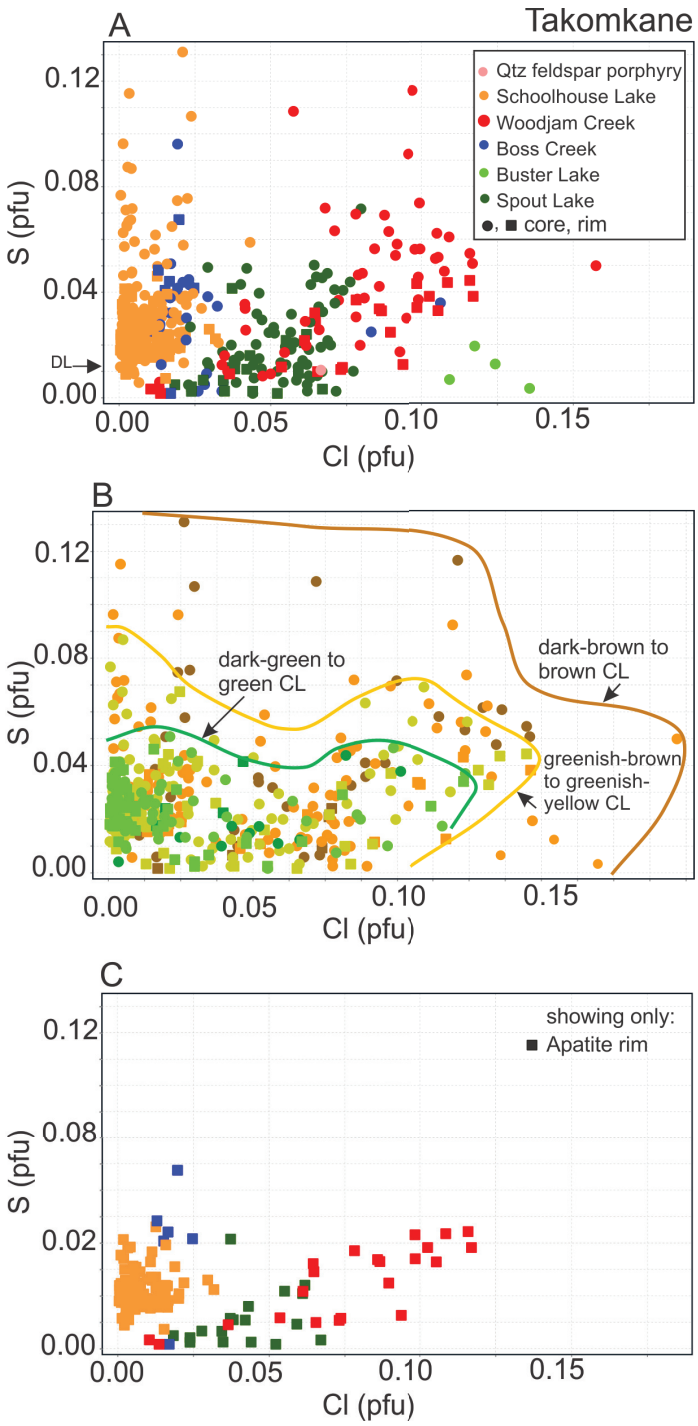

Figure 16: (a) Chlorine and sulphur variation in apatite from Takomkane batholith. (b) Same diagram as in Fig. 16a but showing the luminescence color of grains. (c) Same as in Fig. 16a but showing only results from the apatite rim.

negative Eu anomaly. Normalized La/Sm and Dy/Yb binary plots are used to show the relative concentration of LREE/MREE and MREE/HREE, respectively (Fig. 19). At Guichon Creek, there is an inverse correlation between $(La/Sm)_n$ and $(Dy/Yb)_n$ in apatite (Fig. 19a). This relationship occurs in apatites from all rock units. However, earlier phases, especially Guichon and Chataway, have some apatite with higher LREE/MREE, $(La/Sm)_n>15$, relative to the mineralized phases such as Bethlehem, $(La/Sm)_n<15$ or Bethsaida, $(La/Sm)_n<5$. When comparing the main mineralized phases, the Bethsaida and Skeena have apatites with higher MREE/HREE, $(Dy/Yb)_n$ up to 2.3, relative to those of Bethlehem with $(Dy/Yb)_n<1.8$ and mostly below 1.5. The exception are a few analyses of Bethsaida phase apatite that have $(Dy/Yb)_n$ of ~ 1. Thus, even though there is considerable overlap, the mineralized phases are depleted in LREE relative to MREE (lower La/Sm), and are slightly enriched in MREE relative to HREE (higher Dy/Yb) whereas the non-mineralized phases display a scatter from high to low.

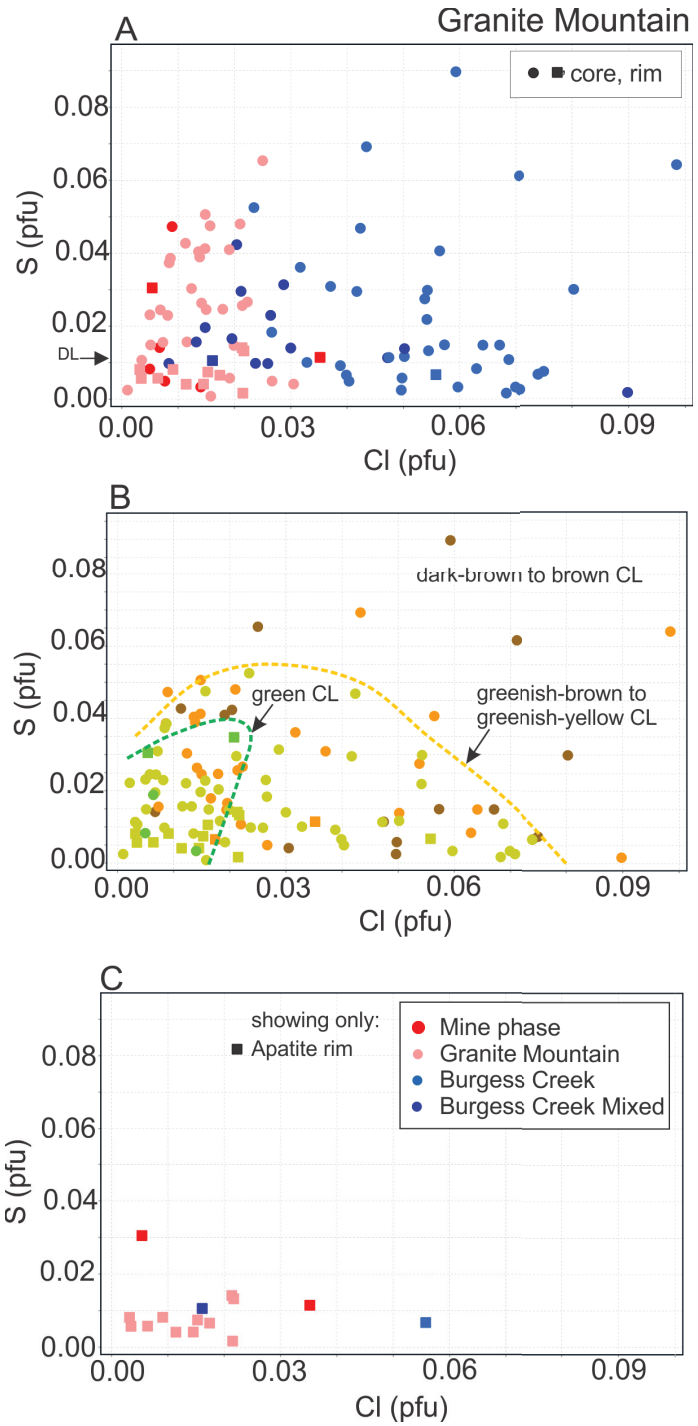

Figure 17: (a) Chlorine and sulphur variation in apatite from the Granite Mountain batholith. (b) Same diagram as in Fig. 17a but showing the luminescence color of grains. (c) Same as in Fig. 17a but showing only results from the apatite rim.

Similar relationships can be seen for REE in apatites from the Takomkane batholith (Fig. 19b) in which apatites from the Woodjam Creek unit have lower LREE/MREE, $(La/Sm)_n$<5, and higher MREE/HREE, $(Dy/Yb)_n$>1.3, relative to other phases. The, apatites from the Boss Creek and Buster Lake display more scattered REE distributions and apatites from the Spout Lake and Schoolhouse Lake plutons have distinctly lower MREE/HREE, $(Dy/Yb)_n$<ca.1.3, and slightly higher LREE/MREE, $(La/Sm)_n$ mostly above 4.

At Granite Mountain, the REE distribution among various plutonic phases does not show distinct variations in LREE/MREE with $(La/Sm)_n$<5 similar to those mineralized phases at Guichon Creek and Takomkane. The Burgess Creek and the Granite Mountain phases tend to have variable Dy/Yb whereas the Mine phase have $(Dy/Yb)_n$>1.4 similar to those at Woodjam (Fig. 19c).

Except for a few analyses, all apatites from the studied batholiths have negative Eu anomalies (Fig. 20). Data also shows a positive correlation between the Eu anomaly and $(La/Sm)_n$. Thus, samples with lower $(La/Sm)_n$ have a more pronounced negative Eu anomaly (i.e., smaller Eu_N/Eu_N*). At Guichon Creek, the earlier phases of Border, Guichon and Chataway, commonly show a variable Eu anomaly from ca. 1.5 to 0.1 whereas Eu anomaly in the mineralized phases progressively decreases from Bethlehem to Bethsaida phase with the latter showing a Eu anomaly between ca. 0.3 to 0.5 (Fig. 20a). Similar relationships occur at Takomkane batholith in which apatites from the Woodjam Creek unit have a lower Eu anomaly (0.2 to 0.4) whereas other phases show variable Eu from 0.1 to 0.8 except for the Schoolhouse Lake unit which has a Eu anomaly of >0.4 (Fig. 20b). At Granite Mountain, apatites of the Mine phase have Eu anomalies of 0.4-0.55, similar to those in Bethsaida, and the other phases have Eu anomalies of < 0.3. Thus, apatites with variable Eu anomalies in the largely barren phases at Guichon Creek and Takomkane do not occur at Granite Mountain (Fig. 20c).

TITANITE COMPOSITION

Iron, Aluminum and Manganese in Titanite

Titanite can incorporate cations into its structures such as Fe^{2+}, Mn^{2+}, Na^{+}, K^{+}, Al^{3+}, Fe^{3+}, Zr^{4+} and REE^{3+}. Fe and Al substitute for Ti and this requires a coupled substitution such as $Ca^{2+} + Ti^{4+} \leftrightarrow REE^{3+} + (Al, Fe)^{3+}$ (Green and Pearson 1986; Enami et al. 1993). Mn^{2+} substitutes for Ca. The Al^{3+} and Fe^{3+} substitutions in titanite are controlled by oxygen fugacity and pressure (Kowallis, 1997). Titanite from the studied batholiths have distinct compositional variations with regard to Fe, Al and Mn (Table 3). The total Fe oxide concentration in titanite varies from 0.3 to 2.7%, for Al_2O_3 from 0.5 to 3.5% and for MnO from below detection (ca. 0.07%) to 0.4%. The data show a positive correlation between the Fe:Al and Mn:Ca ratios (Fig. 21). At Guichon Creek (Fig. 21a), titanite from the Border phase has the lowest Fe:Al (<1.2) and Mn:Ca (<0.005) whereas the Guichon, Chataway and Bethlehem phases display higher ratios. Titanites from the Skeena phase show slightly higher ratios and the Bethsaida phase typically has the highest Fe:Al (>1.3) and Mn:Ca (>0.07) ratios.

In general the Fe:Al and Mn:Ca ratios in titanite increase from the Border phase towards the central mineralized Bethsaida phase. At Takomkane batholith, titanite compositions display a large overlap (Fig. 21b). All phases of the batholith display Fe:Al ratios of mostly <1.1 and Mn:Ca ratios of largely <0.007 except for a small number of analyses from the Schoolhouse

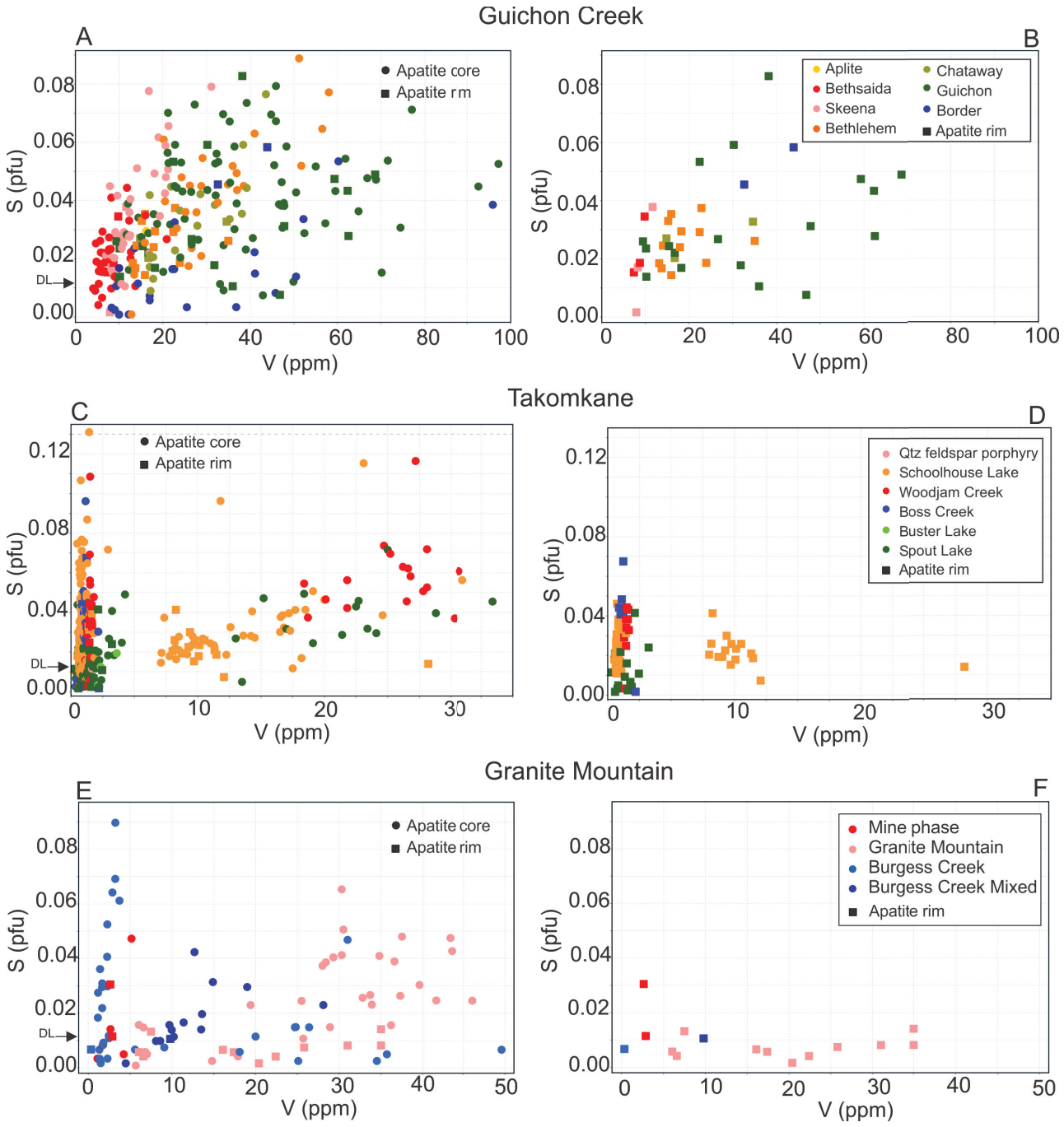

Figure 18: Vanadium variation in apatite from Guichon Creek (A, B), Takomkane (C, D) and Granite Mountain (E, F) batholiths. The left panels show all analyses; the right panels show only apatite rim analyses.

Lake, and the majority of those from the mineralized Woodjam Creek unit. Most of the titanites from the Woodjam Creek unit show distinctly higher Fe:Al ratios (>1.1). Therefore, despite the overlaps, titanites from the Woodjam Creek are characterized by higher Fe:Al ratio relative to other phases of the batholith.

REE in Titanite

The REE concentrations in titanite (Table 3) are characterized by using normalized La/Sm and Dy/Yb, and the calculated Eu anomaly. REE partitioning in titanite is similar to that in apatite (Sha and Chappell, 1999), characterized by higher LREE and MREE concentration relative to HREE—therefore similar relationships are expected. At Guichon Creek (Fig 22a), there is an inverse correlation between $(La/Sm)_n$ and $(Dy/Yb)_n$ in titanite (Fig. 22a) for all rock units. There is considerable overlap in titanite REE amongst various phases but the mineralized phases of the Bethlehem, Skeena and Bethsaida do not have high LREE/MREE, $(La/Sm)_n$ are below 5 and thus similar to the ratios of those in apatite. The highest MREE/HREE ratios, $(Dy/Yb)_n$>1.5, are also in titanites of the Bethsaida phase. At Takomkane (Fig. 22b), the Schoolhouse Lake pluton and Quartz-Feldspar Porphyry unit

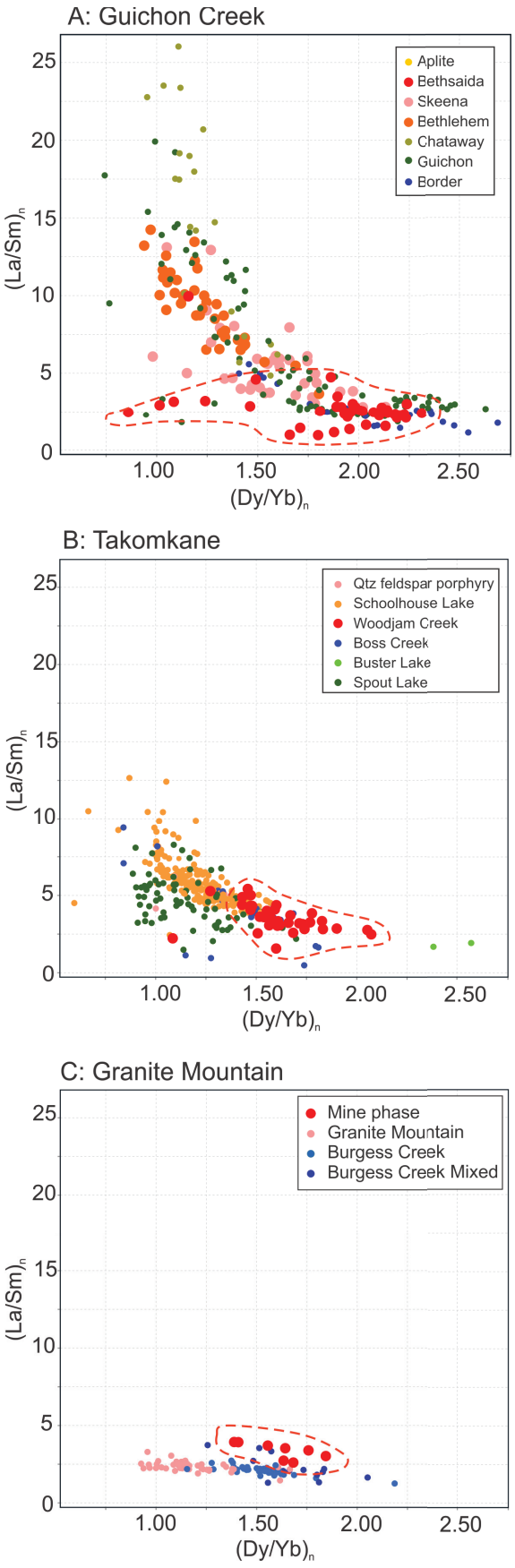

Figure 19: (left) REE characteristics of apatite showing LREE/MREE and MREE/HREE relationships for Guichon Creek (A), Takomkane (B), and Granite Mountain (C) batholiths.

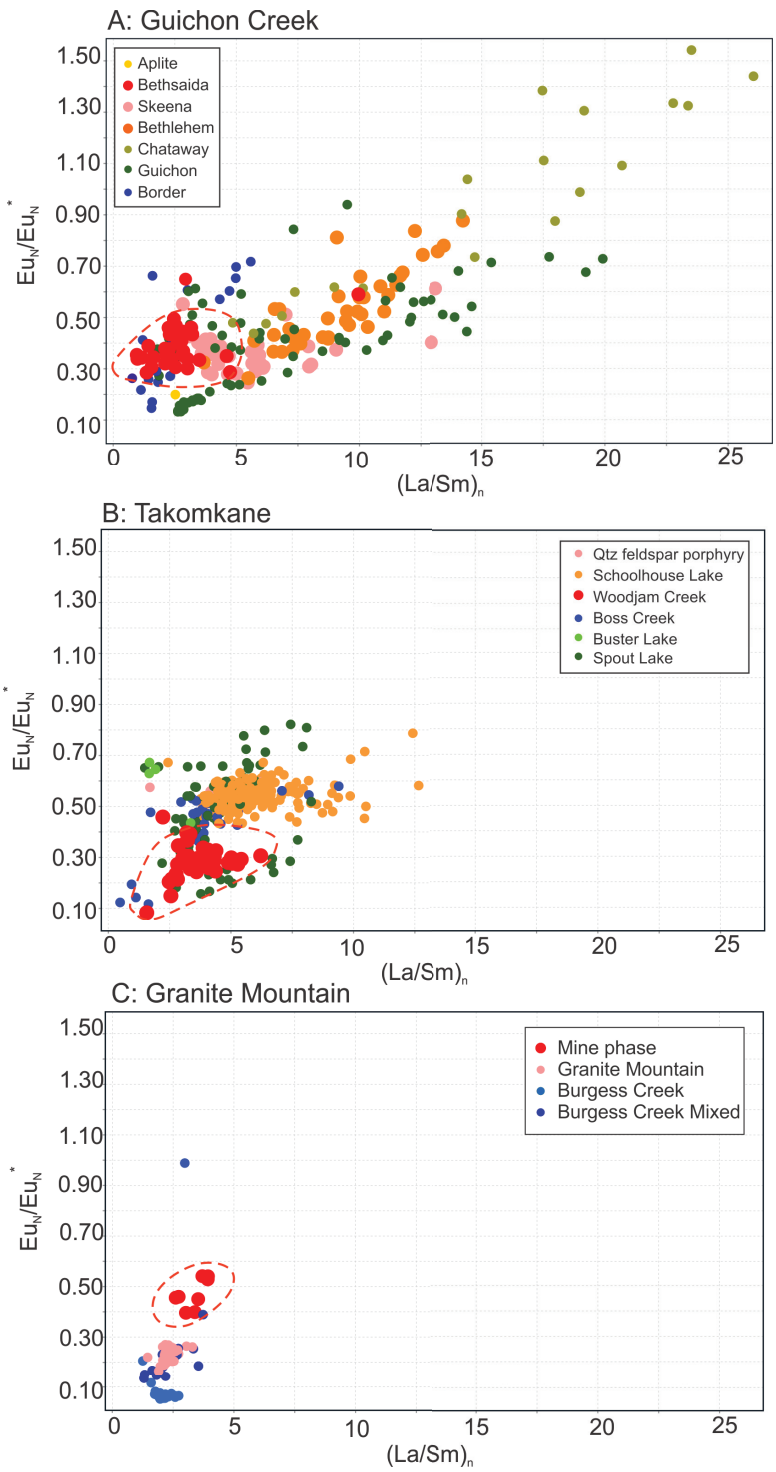

Figure 20: REE characteristics of apatite showing Eu anomaly for Guichon Creek (A), Takomkane (B), and Granite Mountain (C) batholiths.

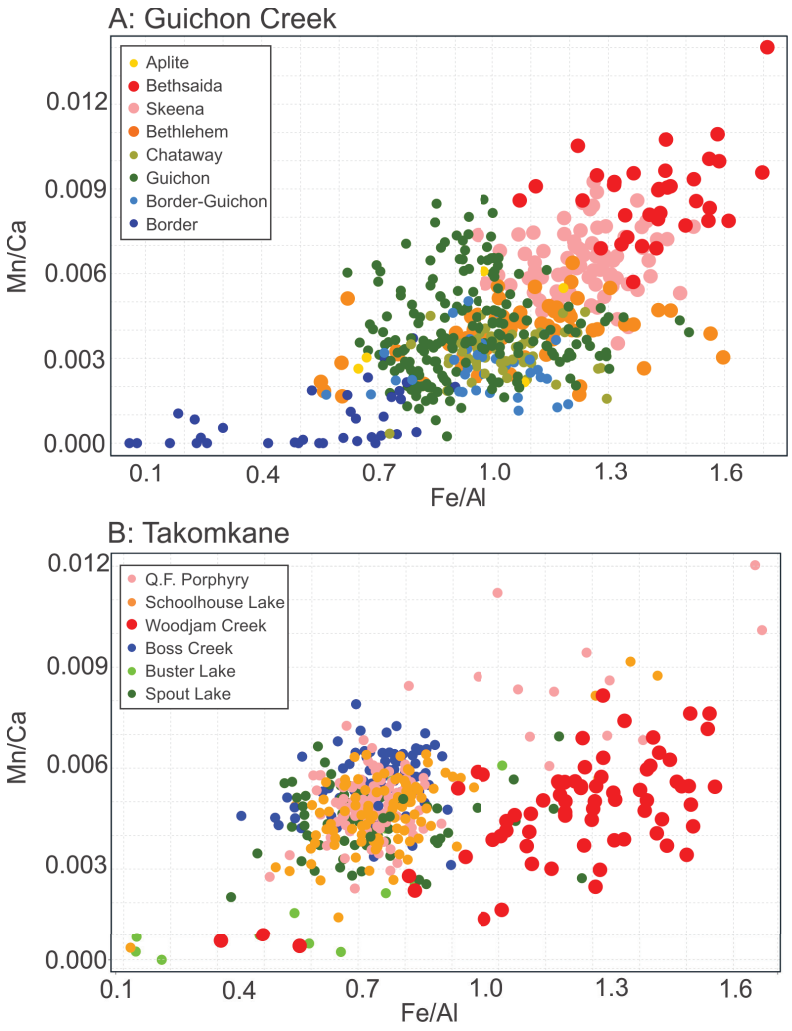

Figure 21: Titanite composition on the basis of Fe/Al and Mn/Ca for Guichon Creek (A) and Takomkane (B) batholiths.

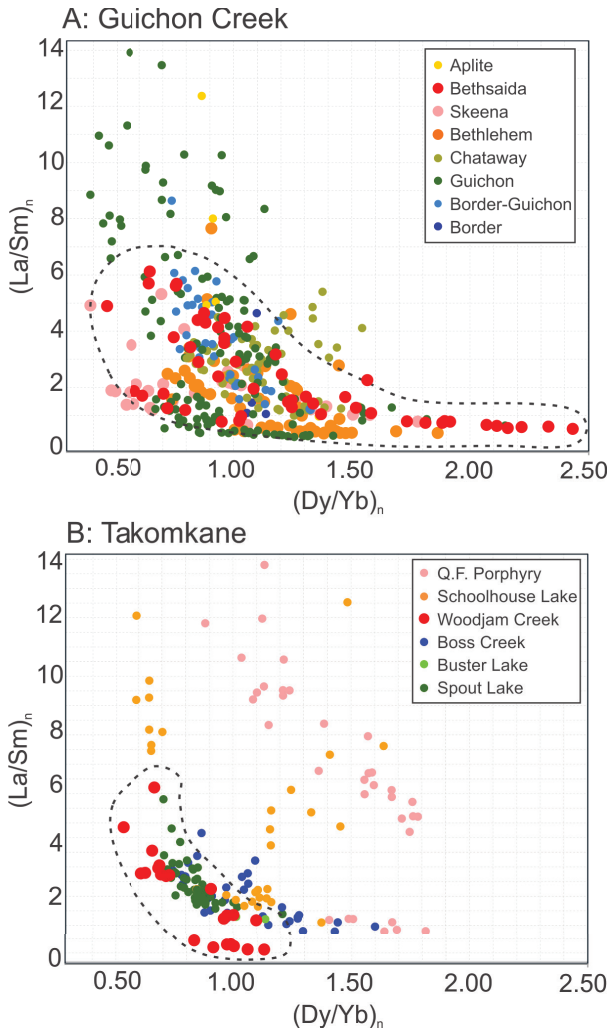

Figure 22: : REE characteristics of titanite showing LREE/MREE and MREE/HREE relationships for Guichon Creek (A) and Takomkane (B) batholiths.

have scattered $(La/Sm)_n$ and $(Dy/Yb)_n$ ratios typically have higher values relative to other phases. All other phases, including the mineralized Woodjam Creek unit, display overall lower LREE/MREE, $(La/Sm)_n$<5, but with no appreciable MREE/HREE enrichment (the $(Dy/Yb)_n$ between 0.5 and 1). Thus, the main mineralized phase of the Woodjam Creek unit has similar REE characteristics to those of less mineralized phases, especially to those at Spout Lake. Notably different is that some of the lowest $(Le/Sm)_n$ ratios (around 0) occur in the Woodjam Creek unit.

The Eu anomaly characteristics in titanite better distinguish the fertile magmatic phases relative to other REE (Fig. 23). Unlike apatite which shows a negative Eu anomaly, titanite displays a range of Eu anomalies from 0.1 to 3.2, i.e., from strongly negative to strongly positive. More significantly however, the mineralized phases display negative Eu anomalies whereas other phases have a range of Eu from weakly negative to, more typically, positive Eu anomalies. At Guichon Creek (Fig. 23a), titanites from the Bethsaida phase and most of those from the Bethlehem and Skeena phases have a Eu anomaly (Eu_N/Eu_N^*) < 0.75 whereas other phases, including the Border, Guichon and Chataway have Eu anomalies that are > 0.77 and up to 3.2. Similar relationships occur at Takomkane in which titanites from the Woodjam Creek unit have Eu anomalies < 0.75 whereas other phases have Eu anomalies that are typically > 0.75 and up to 3.25.

DISCUSSION

Because porphyry copper deposit formation relies on variables related to the (1) oxidation state, (2) temperature, (3) water, (4) metal, (5) chlorine and (6) sulphur content of the magma (Burnham and Ohmoto, 1980), the identification of these parameters in rocks or minerals provides indications of pluton fertility. Here, we discuss how the studied textural and compositional characteristics of apatite and titanite help to identify some of such parameters.

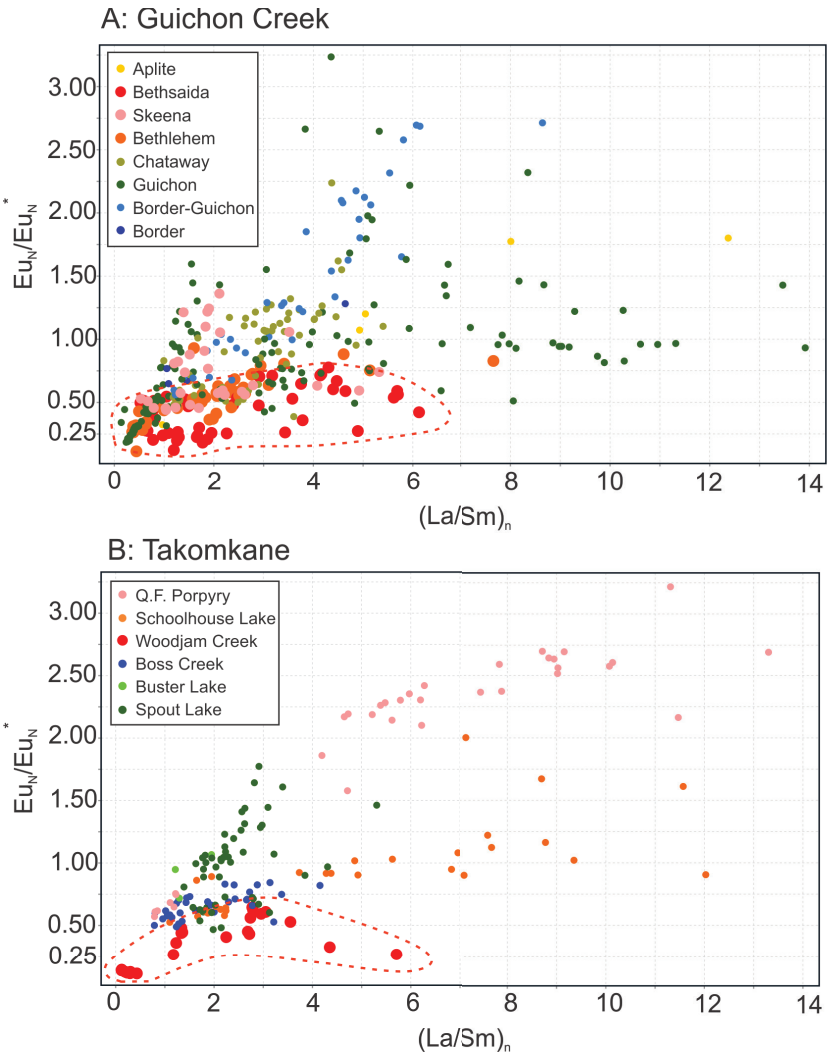

Figure 23: REE characteristics of titanite showing Eu anomaly for Guichon Creek (A) and Takomkane (B) batholiths.

Fractional Crystallization and Potentially Fluid Exsolution Evidence from Low La/Sm and high Dy/Yb

Porphyry-fertile plutonic phases such as Bethsaida, Woodjam Creek and the Mine Phase consistently have apatite and titanite with lower LREE/MREE ratios and $(La/Sm)_n$ < 5, relative to those non-mineralized or poorly mineralized phases. This at least partially correlates with a slight increase in MREE/HREE ratio, $(Dy/Yb)_n$ > ca. 1.5. The decrease in LREE in apatite and titanite is attributed to the fractional crystallization of minerals in the silicate melt such as monazite, allanite and other minerals with high LREE partition coefficients (e.g., 100 to 1000 times greater than apatite and titanite: Sha and Chappell, 1999). These minerals deplete the melt in LREE and result in apatite and titanite formation from such melt inheriting a depleted LREE signature.

Fractional crystallization is a common and fundamental process that can result in water saturation and the generation of the substantial volumes of hydrothermal fluid required to produce a porphyry deposit (Burnham, 1979). Field and petrographic evidence from these zoned batholiths that progressively evolve more felsic phases supports this interpretation. Whole rock analyses at Guichon Creek for example, show that mineralized phases are enriched in Sr/Y and depleted in Y (see Fig. 12) indicating that high water pressure suppressed plagioclase and enhanced hornblende crystallization (see above, Rohrlach and Loucks, 2005). Garnet is also favored by high water contents (see Bissig et al., 2017) but garnet does occur in the studied plutons. The slight increase in MREE/HREE in apatite and titanite could be related to the fractionation of zircon which preferentially partially depletes the melt in HREE (Richards, 2012). The MREE enrichment in apatite could also be related more directly to an effect of the exsolved fluids. Krneta et al., (2017) have shown that MREE-enriched apatite represent a magmatic-hydrothermal transition and hydrothermal effects. Such effects could be considered for some of our samples with very high $(Dy/Yb)_n$ (e.g., greater that 1.5 or 2). The depletion of LREE may also be influenced at the onset of hydrothermal stage and fluid exsolution. Migdisov et al., (2016) show that LREE may be preferentially partitioned relative to HREE into the fluids due to the increased stability and solubility as LREE–Cl complexes.

Therefore, several lines of evidence support apatite and titanite LREE depletion and MREE enrichment to result from the process of fractional crystallization which formed felsic melts that become progressively more hydrous and probably resulted in fluid exsolution.

Evidence for the Oxidation State from Eu anomaly and Fe:Al ratio?

Porphyry copper deposits preferentially form from oxidized magmas (e.g., Burnham and Ohmoto, 1980) and lack significant negative Eu anomalies that have widely been interpreted to characterize an oxidized state of the progenitor magma (Lang and Titley, 1998, Loucks, 2014). This is largely because Eu occurs in two oxidation states (Eu^{2+} and Eu^{3+}), and Eu^{2+} favours partitioning into feldspar whereas Eu^{3+} favours apatite or titanite. These ratios can be anomalously positive or negative when compared to a standard. The europium anomaly (Eu_n/Eu^*) is typically calculated as the ratio of chondrite-normalized Eu abundance relative to Sm and Gd. Thus, crystallization from higher fO_2 magmas results in lower Eu^{2+}/Eu^{3+} ratios which in turn results in weak, flat or even positive Eu anomalies in the whole rock, apatite and titanite chemistry.

Mineralized phases from the studied batholiths have apatites and titanites with characteristic Eu anomalies that are <0.6 whereas most from the other

phases have a wide range of Eu anomalies. In particular, the titanites from the non-mineralized or poorly mineralized plutons have distinctly weak negative or even positive Eu anomalies. Similar trends for titanite have been previously shown by Xu et al., (2015). These Eu data suggest that fertile plutons were less oxidized relative to other plutonic phases. This contradicts conclusions from several other studies (e.g., Lang and Titley, 1998; Richards, 2012; Loucks, 2014) as well as results from whole rock data presented here showing that mineralized plutons typically have flat Eu anomalies which could result from a high magmatic oxidation state. More importantly, the Fe:Al ratios of titanite strongly suggests that fertile plutons were more oxidized than other plutons. These plutons have titanite with higher Fe:Al and Mn:Ca ratios. The Fe^{3+} substitution in titanite is controlled by oxygen fugacity and high fO_2 increases the proportion of Fe^{3+} that substitutes into the Ti-site thus causing higher Fe:Al (Kowallis, 1997).

We interpret that observed Eu anomalies in apatite and titanite are affected by factors other than oxidation state. The high positive Eu anomaly, particularly in titanite, suggests that these minerals formed from a melt that was enriched in Eu, probably as a result of influx of hot, mafic melt which melted plagioclase-rich rocks. As titanite and apatite crystalized from such a melt, they progressively scavenged Eu from the melt. The partition coefficients (K_D) of Eu^{3+} in titanite and apatite are significantly greater than for Eu^{2+}. For titanite, the K_D for Eu^{2+} is 0.37 whereas for Eu^{3+} is about 1000 (Bachmann et al., 2005). Apatite has similar K_D values (Sha and Chappell, 1999). This results in less Eu^{3+} and an increase in the Eu^{2+}/Eu^{3+} ratio of the residual melt as titanite and apatite fractionate causing the trend of depleting Eu in apatite and titanite with decreasing $(La/Sm)_n$. The crystallization of titanite and apatite will also affect Eu anomaly in other co-crystalization phases such as zircon as shown by Loader et al., (2017).

This process probably has negligible effect on the Eu anomaly of the whole rock which is controlled mostly by plagioclase fractionation and Eu^{2+} abundance. Thus, as the melt goes through fractional crystallization and water pressure of the residual melt increases, plagioclase crystallization is suppressed to generate a rock with a less negative Eu anomaly, as observed from the whole rock data. During these final magmatic processes and at the onset of water saturation and hydrothermal stages, titanite and apatite scavenge the little remaining Eu^{3+} whose abundance would be even more depleted if phases such as monazite and zircon and to lesser degree amphibole were crystalizing.

Therefore, we suggest that the observed Eu anomaly in titanite and apatite in the evolving magma does not reflect the oxidation state of the magma, and that its characteristics are more dependent on the fractionation of titanite and apatite, and perhaps is also influenced by other phases such as zircon and monazite. Instead of considering or utilizing the Eu anomaly, we suggest that other ratios such as Fe:Al in titanite can provide a more robust indication of the oxidation state when using mineral chemistry data.

Sulphur and Chlorine: Evidence for Fertile and Degassed Magmas

Sulphur and Cl are critical magmatic ingredients required to produce porphyry copper deposits. Chlorine is required to complex with Cu to attract and partition the metal from the melt into hydrothermal fluids, and S is needed to deposit sulphide mineralization. Chlorine, with F and OH, occupy a single ion site in apatite. Chlorine partitioning between melt, apatite and fluid is a function of melt composition, pressure and temperature. Chlorine at low pressure (ca. 275 bars) and in rhyolitic melts partitions more strongly in favour of apatite whereas at higher pressures and in more mafic melts, more strongly partitions into fluids (Webster et al., 2009; Webster and Picolli, 2015). Sulphur in oxidized magma occurs as SO_4^{2-} and substitutes for PO_4^{3-} in apatite whereas in reduced magmas occurs as S^{2-} and precipitates as sulphide (Sha and Chappell, 1999). Therefore, sulphur-rich apatite reflects formation in oxidized magmas.

Apatite from Guichon Creek, Takomkane and Granite Mountain batholiths have high concentrations of S and Cl, particularly in the magmatic phases that were emplaced prior to the main phases that host mineralization. This is best exemplified by S- and Cl-enriched apatite that forms the Border, Guichon and Chataway phases of the Guichon Creek batholith, and in the Burgess Creek and Burgess Creek Mixed border phases of the Granite Mountain batholith. The main mineralized phases of these batholiths, such as Bethsaida and the Mine Phase, have apatites with lower S and Cl concentrations. Moreover, zoned apatites from mineralized phases have remnant cores of the apatite with higher S and Cl concentrations that typically have brown luminescence whereas the green luminescent rims are depleted in Cl and S. Takomkane batholith apatites have slightly different characteristics. The Woodjam Creek unit, host rock of the largest porphyry deposits in the batholith, has apatites with variable S and Cl concentrations and positive correlation between S and Cl. Similar relationships is seen with those from the older Spout Lake pluton which hosts several smaller porphyry occurrences. Notable different are the weakly mineralized Boss Creek and Schoolhouse Lake plutons that have low Cl and variable S concentrations.

These data indicate that the parental magmas of the three batholiths had high and perhaps sufficient S and Cl to generate porphyry copper deposits. Evidence of high S and Cl melts is recorded in apatite from the pre-mineralization plutonic phases, and locally at the cores of the apatites from the mineralized plutonic phases. More significant indicators of the formation of porphyry deposits are the occurrences of plutons and plutonic phases with Cl- and S-depleted apatites which we interpret to result from aqueous fluid exsolution and degassing of Cl- and

S-phases. During these processes, Cl and S are extracted from the melt and transported by the fluids and gases resulting in apatites crystalizing from these depleted melts with lower S and Cl concentrations. The low Cl but variable S concentration in Bethlehem and to lesser extent at Bethsaida suggest that the S and Cl depletions in apatite may have been controlled by slightly different processes. Thus, Cl depletion was probably more related to water phase exsolution whereas S more dependent on other volatile exsolution.

Dilles (1987) argued that cooling and degassing of the melt can effectively strip Cl and S from the apatite. The depletion in S is attributed to the evolution of an oxidized early magma that is SO_4-rich to a melt that is SO_4-poor as a result of crystallization of anhydrite (Streck and Dilles, 1998). Economos et al., (2017) also suggested degassing as a possible reason for the occurrence of apatite with low S concentration at the rims. Thus, the depletion in both Cl and S of apatite from the mineralized pluton provides evidence for fluid exsolution and degassing of SO_2-rich magmatic volatiles from SO_4-rich melts. Overall, these Cl- and S-rich aqueous and gaseous phases that are generated from fertile magmas are ideal and essential components in the formation of porphyry copper deposits.

An important variable to consider is that the apatites of the Bethsaida phase are largely depleted in S and Cl (except some cores), whereas apatites of the Woodjam Creek unit have a trend of S and Cl from high to low. This may suggest that fluid exsolution and degassing occurred in the Bethsaida phase during much of its evolution, whereas such processes at the Woodjam Creek unit occurred only after some degree of crystallization. Also the similarity of the apatite in the Woodjam Creek plutonic phases with larger porphyry deposits, with apatites from the Spout Lake pluton which hosts several smaller porphyry occurrences, suggests that apatite composition alone may not indicate the magnitude of the mineralization. Factors additional to S and Cl concentrations need to be considered.

It is important to note that other factors may influence the S and Cl concentrations in apatite, but when combined with other data the fertility of these grains can be fully recognized. The Schoolhouse Lake pluton for example, contains apatites with low S and Cl concentration and locally S- and Cl-rich cores. Such low Cl and S apatite may suggest that the parental melt was largely poor in the Cl and S and therefore not porphyry-fertile. Moreover, the lack of appreciable mineralization within the Schoolhouse Lake phase could be related to the deeper erosion of this unit as a large body in the center of the batholith relative to the Woodjam Creek unit which occurs at the margin of the batholith. Narrow shear zone-type copper veins at Schoolhouse Lake pluton supports that the exposed parts of this unit represents a deeper part of the batholith. Even though the apatites from the Schoolhouse Lake pluton may resemble those from Bethsaida, results from the titanite Fe:Al (< 1) indicates that the Schoolhouse Lake is distinctly less oxidized relative to the Woodjam and Bethsaida phases. Thus, a combination of S and Cl in apatite *and* Fe:Al in titanite provides better proxy for fertility.

CONCLUSIONS

Results from investigations of whole rock geochemistry, and apatite and titanite characteristics from porphyry copper deposit plutonic host rocks suggests that several key porphyry fertility parameters can be identified:

1) Fertile plutonic rocks are preferentially part of lithologically-zoned batholiths with more mafic marginal phases. Fertile batholiths have lithologies that evolve from gabbro to granodiorite to granite and a change of >20 wt% SiO_2. Lithologies that are most strongly associated with mineralization have 62 to 72 wt% SiO_2. These more fertile rocks tend to be more sodic than potassic, and are enriched in Al_2O_3, particularly with respect to TiO_2. Trace element geochemistry is characterized by higher Sr/Y (>50) attributable to high dissolved water contents of the melt which suppresses plagioclase crystallization. Most samples have moderate LREE enrichments (La/Sm_n > 2), and moderate MREE enrichments that indicate that hornblende (and/or garnet) crystallization dominated. They lack significant negative Eu anomalies which also emphasizes a hydrous melt that suppressed plagioclase crystallization.

2) Apatites in the studied samples have brown, green or yellow luminescence. Concentric zoning is common with alternating zones of dark-brown, brown, greenish-brown and green luminescence. In many samples, light brown cores are surrounded by darker brown zones. Green luminescent rims are common. Apatite in unmineralized rocks has uniform to zoned brown luminescence. The green-luminescent apatite typically has dark brown cores that are zoned outward to green-brown and green-luminescent apatite. Apatite grains in mineralized units tend to have well-developed green luminescence. Spot analysis indicates that the brown luminescent cores have higher Cl and S relative than the green luminescent rims.

3) Apatite and titanite from the fertile plutons are characterized by LREE depletion ($(La/Sm)_n < 5$) and commonly MREE enrichment ($(Dy/Yb)_n$ > ca. 1.5). This is interpreted to have resulted from fractional crystallization and fluid exsolution. Fluid exsolution is a key process for the formation of the porphyry copper deposits and is dependent on a melt's initial water content and fractional crystallization (Burnham, 1979).

4) Apatite and titanite from the fertile plutons are characterized by an elevated oxidation state. The Eu anomaly of apatite and titanite from fertile plutons is distinct, typically <0.6. Results from this study show that the Eu anomaly in apatite and titanite is not a robust indication of the oxidation state but rather that it is influenced by fractional crystallization. The Fe:Al ratio of

titanite, however is an alternate and more robust indication of the oxidation state with fertile plutons having Fe:Al >1.

5) Apatite from the fertile plutons are characterized by cores with high, elevated concentrations of sulphur (>0.3 wt.% oxide) and chlorine (> 0.35 wt.% oxide) and rims that are low and depleted in S (< 0.3 wt.%) and Cl (< 0.35 wt.%) with most results below detection limit. Barren plutons may show S- and Cl-enriched apatite but lack significantly S- and Cl-depleted apatites. The S- and Cl-depleted apatites are characterized by greenish-brown to green luminescence colours whereas S- and Cl-enriched apatites are characterized by brown luminescence colour. The S- and Cl-depleted apatite suggests that melt was originally enriched in these components but lost much of its Cl and S to the generation of exsolved fluids which upon ascent could generate porphyry copper deposits.

While the identification of the fertility factors in apatite and titanite such as crystal fractionation, high oxidation state and water content, fluid exsolution, and S and Cl concentrations are important for recognizing a magma's potential for porphyry mineralization, any of the criteria outlined above does not by itself indicate porphyry-fertile magma with certainty. Rather, several or all the criteria discussed here should be present. For example, the Bethsaida, Woodjam and the Mine phase plutons which are known mineralizers have all of the favourable indicators including S and Cl concentrations in texturally-distinct apatite, low LREE/MREE and high MREE/HREE in both apatite and titanite and high Fe:Al in titanite (i.e., more oxidized). Other barren, non-mineralized or poorly mineralized plutons lack all or some of the fertility criteria discussed herein. Therefore, a robust fertility tool kit (Table 4) should be used to assess multiple factors in the geology, lithogeochemistry and multiple mineral phases. Plutons that have these factors have higher potential to host porphyry type mineralization.

ACKNOWLEDGMENTS

Geoscience BC is thanked for its financial contribution in support of this project. Additional samples from the Granite Mountain batholith were provided by P. Schiarizza of the BC Geological Survey and N. Mostaghimi of The University of British Columbia. Bahram Najafian helped with mineral separation. Luana Yeung helped with rock and grain photography and drafting maps. Eric Chan and Haley McIntyre assisted with microprobe and LA-ICP-MS analysis, respectively. Mati Raudsepp and Edith Czech from the EOAS probe lab and Marghaleray Amini from the Pacific Center for Isotopic and Geochemical Research (PCIGR) labs are thanked. Johanna McWhirter assisted with review and editing. Sara Jenkins assisted with the final figures and layout.

Table 4: Porphyry Copper Fertility Tool Kit: geological, lithogeochemical and mineralogical features that contribute to enhanced porphyry copper deposit fertility in calc-alkaline plutonic rocks.

Feature	Pluton 1	Pluton 2	Pluton 3
Geology			
Batholith in Quesnellia			
Late Triassic – Early Jurassic age			
Elongate shaped batholith			
NNW trend			
>15 km long axis			
Concentric zonation of lithologies			
Gabbroic to granitic compositions			
SiO_2 ca. 50 to 72 wt.%			
Hornblende and titanite bearing			
Lithogeochemistry of most fertile phases			
SiO_2 ca 62 to 72 wt.%			
TiO_2<0.5			
$Na_2O>K_2O$			
Al_2O_3 enriched			
Sr/Y >50			
moderate LREE enrichments La/Sm_n > 2			
weak MREE enrichments relative to HREE (Dy/Yb_n = 1 to 1.5)			
Weak to no negative Eu anomaly			
Apatite Characteristics			
Zoned luminescence patterns			
Dark brown luminescence cores with green rims			
Abundant grains with green luminescence			
Elevated Cl (>0.35 wt.% oxide) and S (>0.3 wt.% oxide) in cores			
Depleted Cl and S rims			
Below detection Cl and S rims			
LREE depletion $(La/Sm)_n$<5			
MREE enrichment $(Dy/Yb)_n$>1.5			
Titanite Characteristics			
Elevated oxidation state, Fe/Al>1			
LREE depletion $(La/Sm)_n$<5			
MREE enrichment $(Dy/Yb)_n$>1.5			
Total	/28	/28	/28

REFERENCES

Ash, C.H., Rydman, M.O., Payne, C.W. and Panteleyev, A., 1999, Geological setting of the Gibraltar mine, south-central British Columbia (93B/8, 9); *in* Exploration and Mining in British Columbia 1998, BC Ministry of Energy and Mines, BC Geological Survey, p. A1–A15.

Audetat, A., and Simon, A.C., 2012, Magmatic controls on porphyry copper genesis: *in* Hedenquist, J.W., Harris, M., and Camus, F.; Geology and Gensis of Major Copper Deposits and Districts of the World: a tribute to Richard H. Sillitoe, Economic Geology Special Publication Number 16; Society of Economic Geologists, p. 553–572

Bachmann, O., Dungan, M.A., Bussy, F., 2005, Insights into shallow magmatic processes in large silicic magma bodies: the trace element record in the Fish Canyon magma body, Colorado: Contribution to Mineralogy and Petrology, v. 149, 338–349.

Bouzari, F., Hart, C.J.R., Bissig, T. and Barker, S., 2016, Hydrothermal alteration revealed by apatite luminescence and chemistry: a potential indicator mineral for exploring covered porphyry copper deposits; Economic Geology, v. 111, p. 1397–1410

Bissig, T., Leal-Mejia, H., Roger, B.S., and Hart, C., 2017, High Sr/Y Magma Petrogenesis and the link to porphyry mineralization as revealed by garnet-bearing I-Type granodiorite porphyries of the middle Cauca Au-Cu belt, Colombia: Economic Geology, v. 112. P. 551-568.

Burnham, A.D., Berry, A.J., Halse, H.R., Schofield, P.F., Cibin, G., and Mosselmans, J.F.W., 2015, The oxidation state of Eu in silicate melts as a function of oxygen fugacity, composition and temperature: Chemical Geology, v. 411, 248–259.

Burnham, C.W., 1979, Magmas and hydrothermal fluids, *in* Barnes, H.L., ed., Geochemistry of hydrothermal ore deposits, second edition: Holt, Reinhart and Winston, Inc., New York, p. 71-136.

Burnham, C.W., and Ohmoto, H., 1980, Late-stage processes of felsic magmatism, *in* Ishihara, S., and Takenouchi, S., eds., Granitic magmatism and related mineralization: Mining Geology Special Issue 8, p. 1-11.

Byrne, K., Stock, E., Ryan, J., Johnson, C., Nisenson, J., Alva Jimenez, T., Lapointe, M., Stewart, H., Grubisa, G. and Sykora, S., 2013, Porphyry Cu-(Mo) deposits in the Highland Valley district, south central British Columbia; *in* Porphyry Systems of Central and Southern BC, Tour of Central BC Porphyry Deposits from Prince George to Princeton, J. Logan. and T. Schroeter (ed.), Society of Economic Geologists, Field Guidebook Series, v 44, p. 99–116.

Bysouth, G.D., Campbell, K.V., Barker, G.E. and Gagnier, G.K., 1995, Tonalite trondhjemite fractionation of peraluminous magma and the formation of syntectonic porphyry copper mineralization, Gibraltar mine, central British Columbia; *in* Porphyry Deposits of the Northwestern Cordillera of North America, T.G. Schroeter (ed.), Canadian Institute of Mining, Metallurgy and Petroleum, Special Volume 46, p. 201–213.

Casselman, M.J., McMillan, W.J. and Newman, K.M., 1995, Highland Valley porphyry copper deposits near Kamloops, British Columbia: a review and update with emphasis on the Valley deposit; *in* Porphyry Deposits of the Northwestern Cordillera of North America, T.G. Schroeter (ed.), Canadian Institute of Mining and Metallurgy, Special Volume 46, p. 161–191.

Celis, M.A., 2015, Titanite as an indicator mineral for alkalic Cu-Au porphyry deposits in south-central British Columbia; M.Sc. thesis, The University of British Columbia, 247 p.

Che, X.D., Linnen, R.L., Wang, R.C., Groat, L.A., and Brand, A.A., 2013, Distribution of trace and rare earth elements in titanite from tungsten and molybdenum deposits in Yukon and British Columbia, Canada. Canadian Mineralogist: v. 51, 415-438

D'Angelo, M., Miguel, A., Hollings, P., Byrne, K., Piercey, S., and Creaser, R., 2017, Petrogenesis and Magmatic Evolution of the Guichon Creek Batholith: Highland Valley Porphyry Cu ± (Mo) District, South-Central British Columbia: Economic Geology, v. 112. 1857-1888.

del Real, I., Bouzari, F, Rainbow, A., Bissig, T., Blackwell, J, Sherlock, R., Thompson, J.F.H., and Hart, C.J.R., 2017, Spatially and temporally associated porphyry deposits with distinct Cu/Au/Mo ratios, Woodjam district, central British Columbia: Economic Geology, v. 112, p. 1673–1717.

Dilles, J. H., 1987, Petrology of the Yerington batholith, Nevada: Evidence for evolution of porphyry copper ore fluids: Economic Geology, v. 82, p. 1750–1789.

Dilles, J.H. and Einaudi, M.T., 1992, Wall-rock alteration and hydrothermal flow paths about the Ann-Mason porphyry copper deposit, Nevada: a 6-km vertical reconstruction; Economic Geology, v. 87, p. 1963–2001.

Economos, R., Boehnke, P., and Burgisser, A., 2017, Sulfur isotopic zoning in apatite crystals: a new record of dynamic sulfur behavior in magmas, Geochimica et Cosmochimica Acta, 215, 387-403.

Elliot, J.C., 1994, Structure and chemistry of the apatites and other calcium orthophosphates: Elsevier, Amsterdam, 389 pp. ISBN 0-444-81582-1.

Enami, M., Suzuki, K., Liou, J.G., Bird, D.K., 1993, $Al–Fe^{3+}$ and F–OH substitutions in titanite and constraints on their P–T dependence. European Journal of Mineralogy: v. 5, p. 219–231.

Frost, B.R., and Lindsley, D.H, 1991, Occurrence of iron-titanium oxides in igneous rocks. In, D.H. Lindsley (Ed.), Oxides Minerals: Petrologic and Magnetic Significance. Mineralogical Society of America, Reviews in Mineralogy, v. 25, p. 469-487.

Frost, B.R., Chamberlain, K.R. and Schumacher, J.C., 2000, Sphene (titanite): phase relations and role as a geochronometer: Chemical Geology, 172, 131–148

Green, T.H., and Pearson, N.J., 1986, Rare-earth element partitioning between sphene and coexisting silicate liquid at high pressure and temperature: Chemical Geology, v. 55, p. 105-119.

Harding, B., 2012, The characterization of molybdenum mineralization at the Gibraltar mines Cu-Mo porphyry, central British Columbia: B.Sc. thesis, Queen's University, 52 p.

Holland, H.D., 1972, Granites, solutions, and base metal deposits: Economic Geology, v. 67, p. 281-301.

Hughes, J.M., and Rakovan, J.F., 2015, Structurally robust, chemically diverse: apatite and apatite supergroup minerals: Elements, v. 11, p. 165-170.

Kowallis, B.J., 1997, Compositional variations in titanite: Abstracts with Programs - Geological Society of America, v. 29, p. 402

Krneta, S., Ciobanu, C.L., Cook, N.J., Ehrig, K, 2017, and Kontonikas-Charos, A., 2017, Rare Earth Element Behaviour in Apatite from the Olympic Dam Cu–U–Au–Ag Deposit, South Australia: Minerals, v. 7, p. 1-26.

Lang, J.R. and Titley, S.R., 1998, Isotopic and geochemical characteristics of Laramide magmatic systems in Arizona and implications for the genesis of porphyry copper deposits: Economic Geology, v. 93, p. 138–170.

Loader, M.A., Wilkinson, J.J., Armstrong R.N., 2017, The effect of titanite crystallisation on Eu and Ce anomalies in zircon and its implications for the assessment of porphyry Cu deposit fertility: Earth and Planetary Science Letters 472 (2017) 107–119

Logan, J.M., and Mihalynuk, M.G., 2014, Tectonic controls on early Mesozoic paired alkaline porphyry deposit belts (Cu-Au±Ag-Pt-Pd-Mo) within the Canadian Cordillera: Economic Geology, 109 (4), pp. 827-858.

Loucks, R.R., 2014, Distinctive composition of copper-ore-forming arc magmas; Australian Journal of Earth Sciences, v. 61, no. 1, p. 5–16.

Mao, M., Rukhlov A.S., Rowins, S.M., Spence, J. and Coogan, L.A. (2016): Apatite trace element compositions: a robust new tool for mineral exploration; Economic Geology, v. 111, p. 1187–1222.

McMillan, W.J., Anderson, R.G., Chen, R. and Chen, W., 2009. Geology and mineral occurrences (MINFILE), the Guichon Creek Batholith and Highland Valley porphyry copper district, British Columbia, Geological Survey of Canada, Open file 6079, 2 sheets.

McMillan, W.J., Thompson, J.F.H., Hart, C.J.R., and Johnston, S.T., 1995. Regional geological and tectonic setting of porphyry deposits in British Columbia and Yukon Territory, in Porphyry Deposits of the Northwestern Cordillera of North America, T.G. Schroeter, editor, Canadian Institute of Mining and Metallurgy, Special Volume 46, pages 40-57.

Migdisov, A.A., Williams-Jones, A.E., Brugger, J., and Caporuscio, F.A., 2016, Hydrothermal transport, deposition, and fractionation of the REE: Experimental data and thermodynamic calculations: Chemical Geology, v. 439, p. 13–42

Mostaghimi, N., 2016, Structural geology and timing of deformation at the Gibraltar copper-molybdenum porphyry deposit, south-central British Columbia: M.Sc. Thesis, University of British Columbia, 358 p.

Panteleyev, A., 1978, Granite Mountain project (93B/8); in Geological Fieldwork 1977, BC Ministry of Energy and Mines, BC Geological Survey, Paper 1977-1, p. 39–42.

Piccoli, P., Candela, P., and Rivers, M, 2000, Interpreting magmatic processes from accessory phases: titanite - a small-scale recorder of large-scale processes: Transactions of The Royal Society of Edinburgh-Earth Sciences, v. 91, 257-267.

Pouchou, J.L., and Pichoir, F., 1985, PAP $\phi(\rho Z)$ procedure for improved quantitative microanalysis: in Armstrong, J.T., ed., Microbeam Analysis, San Francisco Press, San Francisco, p.104-106.

Richards, J., 2012, High Sr/Y magmas reflect arc maturity, high magmatic water content, and porphyry Cu ± Mo ± Au potential: examples from the Tethyan arcs of central and eastern Iran and western Pakistan: Economic Geology, v. 107, p. 295–332.

Roegge, J.S., Logsdon, M.J., Young, H.S., Barr, H.B., Borcsik, M., and Holland, H.D., 1974, Halogens in apatite from the Providencia area, Mexico: Economic Geology, v. 69, p. 229-240.

Rohrlach, B. D., and R. R. Loucks, 2005, Multi-million-year cyclic ramp-up of volatiles in a lower crustal magma reservoir trapped below the Tampakan copper-gold deposit by Mio-Pliocene crustal compression in the Southern Philippines, in T.M. Porter, ed., Super porphyry copper and gold deposits – a global perspective: PGC Publishing, 2, 369-407.

Sánchez, M.G., Bissig, T. and Kowalcyzk, P., 2015, Toward an improved basis for beneath-cover mineral exploration in the QUEST area, central British Columbia: new structural interpretation of geophysical and geological datasets (NTS 093A, B, G, H, J, K, N); Geoscience BC Report 2015-15.

Schiarizza, P., 2015, Geological setting of the Granite Mountain batholith, south-central British Columbia; in Geological Fieldwork 2014, BC Ministry of Energy and Mines, BC Geological Survey, Paper 2015-1, p. 19–39,

Schiarizza, P., Bell, K. and Bayliss, S., 2009, Geology and mineral occurrences of the Murphy Lake area, south-central British Columbia (NTS 093A/03); in Geological Fieldwork 2008, BC Ministry of Energy and Mines, BC Geological Survey, Paper 2009-1, p. 169–188.

Schiarizza, P., Israel, S., Heffernan, S., Boulton, A., Bligh, J., Bell, K., Bayliss, S., Macauley, J., Bluemel, B., Zuber, J., Friedman, R.M., Orchard, M.J., and Poulton, T.P., 2013, Bedrock Geology between Thuya and Woodjam creeks, south-central British Columbia NTS 92P/7, 8, 9, 10, 14, 15, 16; 93A/2, 3, 6: British Columbia Geology Open File 2013-05

Sha, L.K., and Chappell, B.W., 1999, Apatite chemical composition determined by electron microprobe and laser-ablation inductively coupled plasma mass spectrometry, as a probe into granite petrogenesis: Geochimica et Cosmochimica Acta, v. 63, p. 3861– 3881.

Sillitoe, R.H., 1973, The tops and bottoms of porphyry copper deposits; Economic Geology, v. 68, p. 799−815.

Sillitoe, R.H., 2010, Porphyry Copper Systems; Economic Geology, 105, 3-41.

Stormer, J.C. Jr., Pierson, M.L., Tacker, R.C., 1993, Variation of F and Cl X-ray intensity due to anisotropic diffusion in apatite during electron microprobe analysis: American Mineralogist, v. 78, 641-648.

Streck, M.J. and Dilles, J.H., 1998, Sulfur evolution of oxidized arc magmas as recorded in apatite from a porphyry copper batholith; Geology, v. 26, p. 523–526.

Sun, S.S., and McDonough, W.F., 1989, Chemical and isotopic systematics of oceanic basalts: implications for mantle composition and processes, in Saunders A.D., and Norry, M.J., eds., Magmatism in the Oceanic Basins: Geological Society of London Special Publication 42, pp. 313-345.

Waychunas, G.A., 2002, Apatite luminescence: in M.L. Kohn, J. Rakovan, and J.M. Hughes (eds.), Phosphates–Geochemical, Geobiological, and Materials Importance: Reviews in Mineralogy and Geochemistry, v. 48, p. 710–742

Webster, J.D., and Piccoli, P.M., 2015, Magmatic apatite: A powerful, yet deceptive, mineral: Elements, v. 11, p. 177–182.

Webster, J.D., Tappen, D., and Mandeville, C.W., 2009, Partitioning behavior of chlorine and fluorine in the system apatite-melt fluid: II. Felsic silicate systems at 200 MPa.: Geochimica et Cosmochimica Acta: v. 73, p. 559-581.

Wones, D.R., 1989, Significance of the assemblage titanite + magnetite + quartz in granitic rocks, American Mineralogist, v. 74, 744–749.

Xu, L., Bi, X., Hu, R., Tang, Y., Wang, X., Xu, Y., 2015, LA-ICP-MS mineral chemistry of titanite and the geological implications for exploration of porphyry Cu deposits in the Jinshajiang – Red River alkaline igneous belt, SW China: Chemical Geology, v. 109, p. 181–200